学位授与年月：**2014.9**

関西大学審査学位論文

STUDIES ON SYNTHESES AND ANALYSIS OF SEMICONDUCTOR NANOSTRUCTURE ARRAYS FOR PHOTOVOLTAIC APPLICATION

Ph.D THESIS

Graduate School of Science and Engineering

Applied Physics Laboratory

By

ChongE WANG
11D6001

Kansai University, Japan
2014

THINK × ACT
KANSAI
UNIVERSITY

STUDIES ON SYNTHESES AND ANALYSIS OF SEMICONDUCTOR NANOSTRUCTURE ARRAYS FOR PHOTOVOLTAIC APPLICATION

Ph.D THESIS

Graduate School of Science and Engineering

Applied Physics Laboratory

By

ChongE WANG
11D6001

SUPERVISOR:
Prof.Shoso SHINGUBARA

September 2014

課程博士

STUDIES ON SYNTHESES AND ANALYSIS OF SEMICONDUCTOR NANOSTRUCTURE ARRAYS FOR PHOTOVOLTAIC APPLICATION

太陽電池応用に向けた半導体ナノ構造体配列の形成と評価に関する研究

関西大学
理工学研究科　総合理工学専攻
応用物理研究室

11D6001
王崇娥

指導教員　　　　新宮原　正三

TABLE OF CONTENTS

Section **Page**

Abstract …..4

Chapter 1 Background of photovoltaic cells

1.1 Basic of photovoltaic cells *.....6*

1.2 Overview of development of photovoltaic cell and materials *.....7*

1.3 Current state of thin film photovoltaic cell *.....9*

1.4 Nanowires photovoltaic cell *.....10*

Chapter 2 Motivation *.....16*

Chapter 3 Characterization methods: Principles and equipments

3.1 Structural characterization methods (XRD, Raman, and TEM) *…..20*

3.1.1 X-ray diffraction (XRD) *…..20*

3.1.2 Raman spectroscopy *..... 22*

3.1.3 Transmission electron microscopy (TEM) *.....23*

3.2 Morphology and composition characterization methods (SEM, XPS, EDX)

3.2.1 Secondary electron microscopy (SEM) *.....24*

3.2.2 Energy-dispersive X-ray (EDX) *.....25*

3.2.3 X-ray photoelectron spectroscopy (XPS) *.....25*

3.3 Optical characterization methods (UV-Vis, PL)

3.3.1 UV-Vis reflection spectroscopy *..... 26*

3.3.2 Photoluminescence spectroscopy (PL) *..... 26*

Chapter 4 Fabrication of vertical Si nanowire arrays

4.1 Vapor-liquid-solid (VLS) method using AAO template *.....29*

4.1.1 Anodic aluminum oxide (AAO) *.....29*

4.1.2 Reduction of pich of AAO nanohole arrays *31*
4.1.3 Formation of AAO on Si substrate *37*
4.1.4 Vapor-liquid-solid (VLS) *38*
4.1.5 Sample preparation *39*
4.1.6 Results *40*

4.2 Self-assembled polystyrene sphere and metal-assisted etching method

4.2.1 Sample preparation *41*
4.2.2 Results *42*

Chapter 5 Fabrication of CZTS absorber layers using cost-effective and Low-environmentally loaded formation technique

5.1 Background *48*
5.2 CIGS and CZTS Crystal Structure *49*
5.3 Electrochemical deposition method *51*
5.4 Sulfurization method with CS_2 .....*55*
5.5 Sample preparation *56*
5.6 Results and discussion *58*
5.6.1 Chemical composition characterization *59*
5.6.2 X-ray diffraction patterns *60*
5.6.3 Raman spectra *61*
5.6.4 Cross-sectional TEM characterization and electron diffraction pattern *62*
5.6.5 Morphological characterization *64*
5.6.6 Carbon element composition characterization *65*
5.6.7 Optical characterization (UV-Vis spectrometer) *67*
5.6.8 Optical characterization (Photoluminescence (PL)) *68*

Chapter 6 Fabrication of CZTS nanostructure arrays using bottom up approaches

6.1 Fabrication of CZTS nanowire arrays

6.1.1 Background *72*

6.1.2 Sample preparation *73*

6.1.3 Results *74*

6.2 Fabrication of CZTS nanocylinders

6.2.1 Background *76*

6.2.2 Mo and CZTS sputtering *77*

6.2.3 Results *77*

Chapter 7 Summary and future work *82*

List of appendices *85*

List of Publications *87*

Acknowledgments *91*

ABSTRACT

In this thesis, mainly three topics about syntheses of semiconductor materials are discussed for photovoltaic applications. First part of the thesis, we prepared the vertical Si(100), (110) and (111) nanowires using Vapor-liquid-solid (VLS) method into anodic aluminum oxide (AAO) template. The crystal orientation of the nanowire could be selected by choosing a Si substrate cut in the desired orientation under the AAO template. Moreover, modifying anodic voltage during AAO preparation, diameter of the nanowire has been controlled. This method allows independent control of the diameter and crystal orientation of the vertically grown epitaxial nanowires.

Second parts, to discuss cost-effective and low environmentally loaded formation technique of photovoltaic cell, electrodeposition and CS_2 sulfurization of CZTS were studied. The single step and two-step electrodepsition of CZTS precursor layer was investigated and compared. The single-step electrodeposition process, where all of the required elements are deposited at once in an electrolyte, has the advantage of simplicity. However, there is a trade-off relationship between the number of processing steps and the ability to control the atomic composition. Therefore, it is difficult to obtain stoichiometric single-phase CZTS using the single-step electrodeposition method. To solve this problem, we used the two-step electrodepositon method. This method has a relatively small number of processes and good controllability of the atomic composition. Sulfurization was performed at several temperatures under CS_2 gas flow. Crystalline and compositional analysis for the CZTS films depending on sulfurization conditions was observed. It is found that the conditions of sulfurization treatment significantly affected the quality of CZTS absorber layer, and suitable formation conditions of CZTS films using this method were decided.

Third part, formation and characterization of nanostructure arrays of CZTS using bottom up approaches were discussed for realization of high efficiency photovoltaic cell. Two types of CZTS nanostructures arrays, in particular nanowires and nanocylinders, were prepared and investigated on morphological and optical properties. Compared with a CZTS film, both of the nanostructured CZTS indicated superior light absorbance properties due to light trapping effect of vertically aligned nanomaterial arrays on substrate.

Moreover, the Structure of glass/Mo/CZTS/CdS/ITO photovoltaic cells using the CZTS as a light absorber layer was prepared.

The study of nanostructure of CZTS absorber layer, nanostructure CZTS absorber layer have an impact on reflectivity and the length of nanocystructure for reflectivity may also be affected. We concluded that CZTS nanostructure to reduce the reflectance and improve the optical have effective. CZTS nanostructure will be apply on the photovoltaic cell is worth waiting for.

CHAPTER 1

BACKGROUND OF PHOTOVOLTAIC CELLS

A photovoltaic cell is an electrical device that converts the energy of light directly into electricity by the photovoltaic effect. When photoelectric cell exposed to light, an electric current is generated without being attached to any external voltage source.

1.1 Basics of Photovoltaic Cells

The basic physics of a photovoltaic cell is found in p-n junction of semiconductor. By combining two types of semiconductor, a p-n junction is formed. When p-type and n-type materials are brought together, electrons flow into the p-type side as a result of diffusion, and similarly holes will flow into the n-type side. As these charged carriers flow an electric field is created by fixed ions. This electric field will cause electrons and holes to flow oppositely as they do under diffusion. At equilibrium condition, diffusion and drift of carrier balance.

Fig. 1.1 shows the most common device structure of thin film photovoltaic cells. The most common substrate is soda-lime glass of 1-3 mm thickness, because it contains Na, which has been shown to yield a substantial open-circuit voltage increase [1], 0.8-1 um molybdenum layer is deposited which serves as the back contact and to reflect most unabsorbed light back into the absorber. Following a p-type absorber layer is grown on Mo with 1-2 um thickness. A thin n-type buffer layer is added on top of the absorber. For CIGS and CIS, the buffer is typically CdS deposited via chemical bath deposition. The buffer is covered with a thin intrinsic ZnO layer, which is capped by a thicker Al doped ZnO layer. The ZnO layer is used to protect the CdS and the absorber layer from sputtering damage during depositing of the ZnO:Al window layer. The Al doped ZnO serves as a transparent conducting oxide to collect and to flow electrons out of the cell.

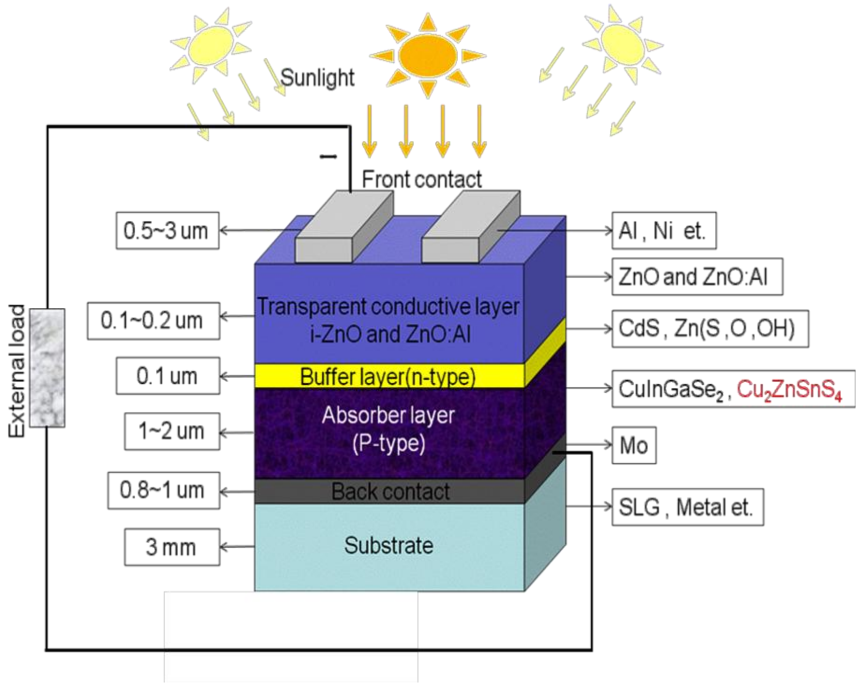

Fig. 1.1 Typical thin film photovoltaic cell structures

1.2 Development of Photovoltaic Cell and Materials Overview

The world's predicted energy demand will reach 28 Terawatt (TW) by 2050 [2]. Meanwhile the earth receives about 10,000 times more energy from the sun than the global energy consumption [3]. In order to meet a sizeable part of the world's demand photovoltaic energy conversion will have to reach TW size.

When the photovoltaic cells were exposed to the light, electric carrier are generated, then together the output voltage and current are harvested by the PV cell, and it can be applied for use by the photovoltaic cell that can then be applied for use.

Over 80% of the photovoltaic market is dominated by technology based on silicon partially due to the maturity of the silicon industry. Si is an indirect band gap material that means it will not absorb incident light efficiently. However, since Si is so widely used in the microelectronics industry, it is still the material of choice as a result of the general expertise of the industry in making devices from Si.

Most photovoltaic cells currently produced are either single crystal Si or polycrystalline Si. Si can be made with high purity resulting in long charge carrier lifetimes due to the absence of defects. As a result of the poor absorption, Si photovoltaic cells must be made thick about 10 um~1 mm to absorb the entire incident light upon them. With the long carrier lifetimes, this is a convenient solution to photovoltaic cell production. Even carriers that are generated far away from the p-n junction will have sufficient time to move to the junction and be separated before recombination occurs. The drawback to this approach is the thick, relatively expensive layers of high purity Si that must be used to produce a working photovoltaic cell. With polycrystalline cells, the cells are cheaper to produce and they can be produced over larger areas. However, the quality of the Si is significantly lower. This results in lower lifetimes for charge carriers. To compensate for this, the approach in polycrystalline Si has been to grow large, high quality grains as cheaply as possible [4] to reduce the cost from single crystal cells while maintaining most of the performance.

On the other hand, there are various alternative approaches that have been researched using other materials. One option is to use high quality group III-V semiconductors to integrate into a concentrating array. The wide band gap semiconductors used are capable of operating under high power conditions. The primary benefit of these systems is to reduce the semiconductor material needed for the cell. The material is high quality and expensive, but a small cell can have greater than 100X light focused onto its surface with no reduction in operating efficiency making this an economical approach. Additionally, multiple junctions can be grown on top of one another to further improve the light collection and efficiency of these devices by tailoring each junction to absorb a specific range of the photovoltaic spectrum.

Another kind of the opposite approach instead of making small, expensive and very efficient photovoltaic cells, in this method thin layers of cheap polycrystalline semiconductor material are used. With these thin film photovoltaic cells the goal is to produce large areas of low quality material cheaply. These materials must have a high absorption coefficient to effectively absorb the entire incident light within the thin layer of the cell. There are three main material systems for this approach. The first is amorphous Si, the most widespread. The other two primary material systems produce high efficiency cells and share much of the same procedures for growth and encapsulation. These materials are CdTe and ($CuInGaSe_2$) CIGS. These materials both have a band gap near the optimum for absorption of the photovoltaic spectrum [5]. Currently, thin film photovoltaic cells are capable of achieving conversion efficiencies of nearly 23%, which compares favorably with amorphous Si as well as polycrystalline Si.

Despite the fact that these materials are used as thin films with thickness varying between 1-2 microns, there may be significant limitations in materials availability and higher cost at TW scale [6,7]. An Earth-abundant and environmentally friendlier version than $CuInGaSe_2$ is Cu_2SnZnS_4 (CZTS) where indium is substituted by tin, gallium by zinc, and selenium by sulfur. CZTS is also a direct band gap semiconductor with band gap reported values between 1.4-1.5 eV [8-11].

To put things in perspective regarding the status and the potential of each technology, Fig. 1.2 shows the best-obtained laboratory cell efficiencies for the different technologies. The best crystalline silicon photovoltaic cells about 27.6% efficiency, the best thin film photovoltaic cells are in the 23.3% range, triple junction photovoltaic cells have reached up to 44.4% efficiency, and the best organic and emerging inorganic photovoltaic cells reach between 8.6 and 17.9% percent.

1.3 Current State of Thin Film Photovoltaic Cell Research

A thin-film photovoltaic cell is that made by depositing one or more thin layers of photovoltaic material on a substrate. The thickness range of such a layer is wide and varies from a few nanometers to tens of micrometers. Thin-film photovoltaic cells are usually categorized according to the photovoltaic material, such as amorphous silicon (a-Si), Cadmium telluride (CdTe), Copper indium gallium selenide (CIGS), and Copper Zinc Tin Sulfur (CZTS) and so on.

Amorphous silicon (a-Si) is the non-crystalline allotropic form of silicon. It can be deposited in thin films at low temperatures onto a variety of substrates. It offers some unique capabilities for a variety of electronics. Cadmium telluride (CdTe) is a stable crystalline compound formed from cadmium and tellurium. It is used as an infrared optical window and a photovoltaic cell material. It is usually sandwiched with cadmium sulfide to form a p-n junction photovoltaic photovoltaic cell. Typically, CdTe photovoltaic cells use an n-i-p structure. CIGS is I-III-VI_2 semiconductor material composed of copper, indium, gallium, and selenium. CIGS is a tetrahedral bonded semiconductor, with the chalcopyrite crystal structure, and a band gap varying continuously from about 1.0 eV to about 1.7 eV.

Among many uses, CIGS is best known as an alternate photovoltaic cell material in thin film photovoltaic cells. In this role, CIGS has the advantages of being able to be deposited on flexible substrate materials, producing highly flexible, lightweight photovoltaic panels. Improvements in efficiency have made CIGS a leader among alternative cell materials. The market for thin film PV grew from 2002 and is still growing rapidly.

CZTS is a quaternary semiconducting compound that has received increasing interest since the late 2000s for applications in photovoltaic cells. The class of related materials includes other I_2-II-IV-VI_4 such as copper zinc tin selenide (CZTSe) and the sulfur-selenium alloy CZTSSe. CZTS offers favorable optical and electronic properties similar to CIGS making it well suited for use as a thin film photovoltaic cell absorber layer, but unlike CIGS, CZTS is composed of only abundant and non-toxic elements. Concerns with the price and availability of indium in CIGS and tellurium in CdTe, as well as toxicity of cadmium have been a large motivator to search for alternative thin film photovoltaic cell materials. Recent material improvements for CZTS have increased efficiency to 11.1% in laboratory cells, but more work is needed for their commercialization [12].

1.4 Nanowires Photovoltaic Cell Research

Specific to the structure of photovoltaic cell, an absorber thickness of roughly 1 to 2 μm is required to ensure high absorption efficiency for the photovoltaic cell. However, this will result in a long diffusion length leading to significant recombination. Nanowire photovoltaic cells offer the potential of significant increase in the absorber efficiency of the cells by decoupling the absorption thickness and the diffusion distance [13].

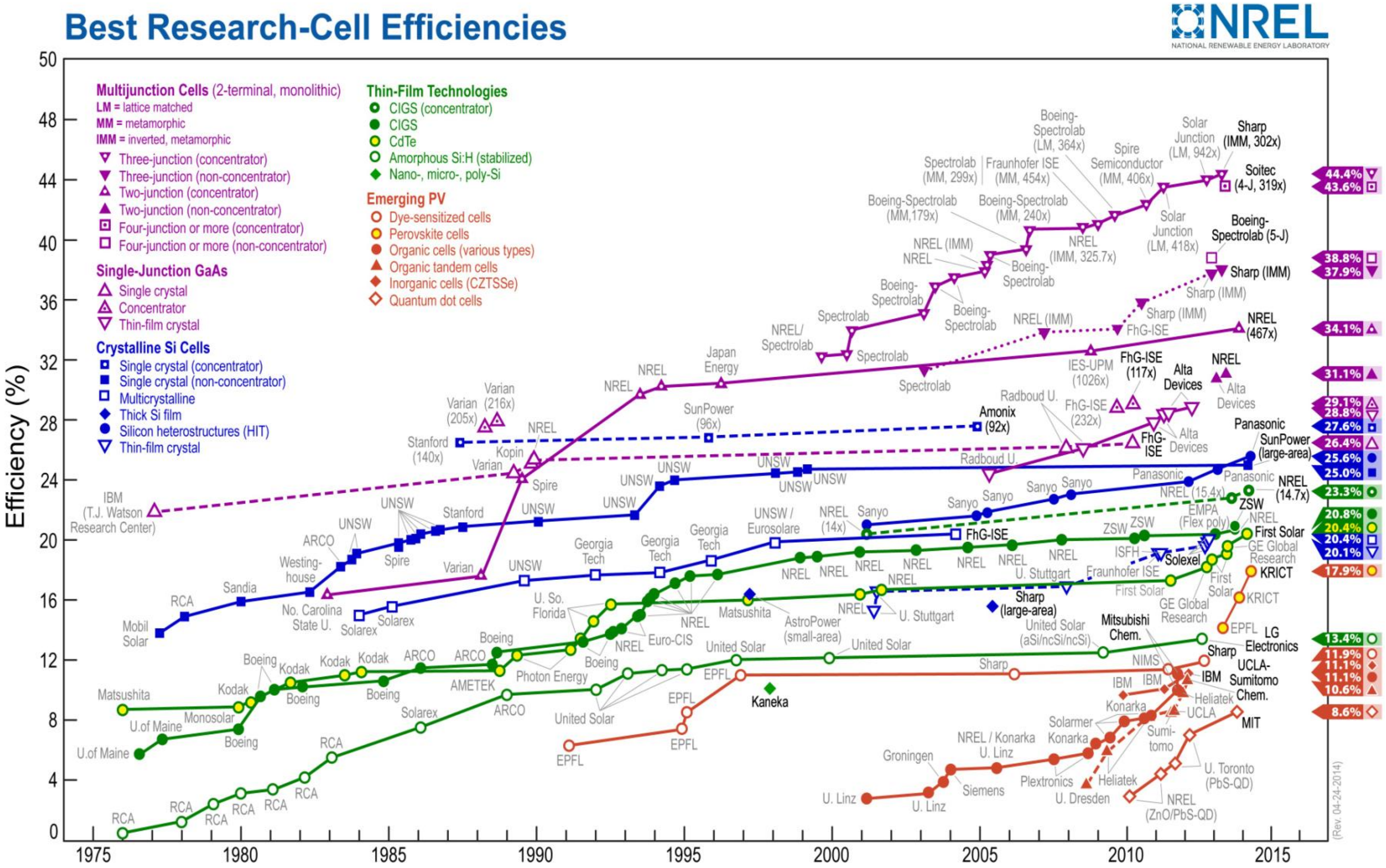

Fig. 1.2 Best laboratory photovoltaic cell efficiencies from the National Renewable Energy Lab in Golden, Colorado

The use of one-dimensional (1D) technology can offer semiconductors a well-aligned morphology with clearly identifiable grain boundaries, where an energy barrier exists and prevents charge carrier recombination [14,15]. In addition, the well-aligned nanowires may provide continuous charge carrier transport pathways. These characteristics would lead to increase in conversion efficiency in the photovoltaic devices [16].

For example, a conventional Si photovoltaic cell consists four main parts: base region, emitter, metallic electrodes, and surface antireflection layer, as depicted in Fig. 1.3. When the device is exposed to light, the photo-generated charge carriers produce a consistent reverse current flow. The surface reflection is one of the most significant factors for optical loss in photovoltaic cells.

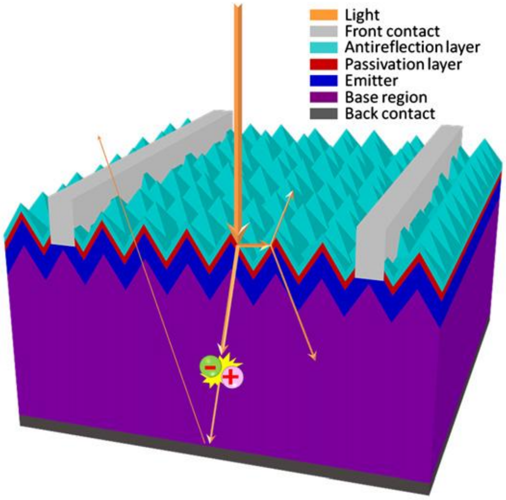

Fig. 1.3 Basic structure of a silicon based photovoltaic cell. [17]

To obtain a lower reflectivity, it is built to high-aspect-ratio wire arrays on the front surfaces of photovoltaic cells since longer light transmission distance are expected due to multiple reflection processes shows in Fig. 1.4 (a) [17]. The light- trapping characteristics of vertically aligned nanowire arrays for PV application are analyzed [18,19–24]. Fig.1.4 (b) shows the absorption spectra of Si nanowires with different length. The thin film counterpart is included as a reference. In the short wave region, the Si nanowire arrays have higher transmittance than the thin films and longer wire length is preferable to expanding the region of the absorption. Therefore, this characteristic would lead to increase in conversion efficiency in the photovoltaic devices.

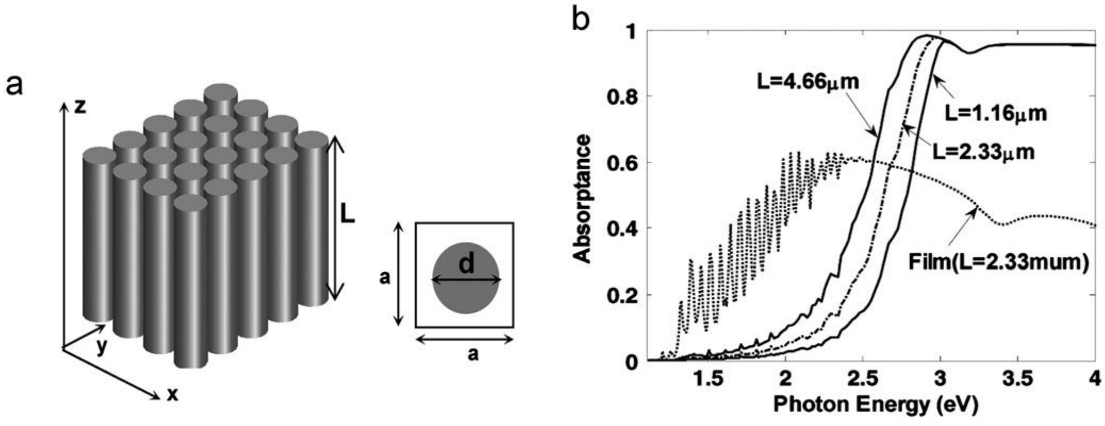

Fig. 1.4 (a) Schematic of a periodic SiNW array. The parameters are the length L, the period a, and the diameter d, respectively. (b) Absorption, spectra of SiNWs with different L. The thin film counterpart is included as a reference. [17]

References of chapter 1

[1] J. Hedström, H. Ohlsen, M. Bodegard, A. Kylner, L. Stolt, D. Hariskos, M. Ruckh, H.W. Schock, Proceedings of 23rd IEEE Photovoltaic Specialists Conference. (1993) 364–371.

[2] M. I. Hoffert, K. Caldeira, A. K. Jain, E. F. Haites, L. D. D. Harvey, S. D. Potter, M. E. Schlesinger, S. H. Schneider, R. G. Watts, T. M. L. Wigley, and D. J. Wuebbles, Nature, 395 (1998) 881

[3] U.S. Department of Energy, Basic Research Needs for Photovoltaic, Energy Utilization (2005).

[4] J. H. Möller, , Semiconductors for Photovoltaic Cells (1993).

[5] I. Visoly-Fisher, S. R. Cohen, A. Ruzin, D. Cahen, Adv. Mater, 16 (2004) 879.

[6] D. B. Mitzi, O. Gunawan, T. K. Todorov, K. Wang, S. Guha, Photovoltaic Energy Materials and Photovoltaic Cells, 17 (2011.1).

[7] J. J. Scragg, P. J. Dale, L. M. Peter, G. Zoppi, and I. Forbes, Phys. Sta. Solid.(b), 245(9) (2008) 1772

[8] Ichimura, Masaya; Nakashima, Yuki. Jpn. J. Appl. Phys, 48(9) (2009) 090202.

[9] H. Katagiri, K. Saitoh, T. Washio, H. Shinohara, T. Kurumadani, S. Miyajima, Photovoltaic Energy Materials and Photovoltaic Cells 65 (2001) 141.

[10] K. Jimbo, R. Kimura, T. Kamimura, S. Yamada, W. S. Maw, H. Araki, K. Oishi, and H. Katagiri, Thin Solid Films, 515 (2007) 5997

[11] K. Ito, T. Nakazawa, Jpn. J. Appl. Phys. Part 1, 27 (1988) 2094.

[12] M. T. Winkler, W. Wang, O. Gunawan, H. J. Hovel, T. K. Todorov, D. B. Mitzi, Energy Environ. Sci., 7 (2014) 1029-1036

[13] B.M. Kayes, H.A. Atwater and N.S. Lewis, Journal of Applied Physics. 97 (2005)114302-1 −114302-11.

[14] M. J. Hetzer, Y. M. Strzhemechny, M .Gao, M. A. Contreras, A. Zunger, L. J. Brillson, Appl. Phys. Lett. 86 (2005) 162105.

[15] H. Peng, D. T. Schoen, S. X. Meister, F. Zhang, Y. Cui, J. Am. Chem. Soc. 129 (2007) 34.

[16] C. Persson, A. Zunger: Phys. Rev. Lett. 91 (2003) 266401.

[17] Tao Song, Shuit-Tong Lee, Baoquan Sun, Nano Energy, 1 (2012) 654-673.

[18] L. Hu, G. Chen, Nano Letters 7 (2007) 3249–3252.

[19] F.J. Garcfa-Vidal, J.M. Pitarke, J.B. Pendry, Physical Review Letters 78 (1997) 4289–4292.

[20] L. Wen, Z. Zhao, X. Li, Y. Shen, H. Guo, Y. Wang, Applied Physics Letters 99 (2011) 143116.

[21] J. Li, H. Yu, S.M. Wong, X. Li, G. Zhang, P.G.-Q. Lo, D.-L. Kwong, Applied Physics Letters 95 (2009) 243113.

[22] C. Lin, M.L. Povinelli, Optics Express 17 (2009) 19371–19381.

[23] J. Li, H. Yu, S.M. Wong, G. Zhang, X. Sun, P.G.-Q. Lo, D.-L. Kwong, Applied Physics Letters 95 (2009) 033102.

[24] J. Li, S.M. Wong, Y. Li, H. Yu, IEEE 35th Photovoltaic Specialists Conference (PVSC), 2010, pp. 001469–001473.

CHAPTER 2

MOTIVATION

Vertically aligned Si nanowires are attracting attention as ideal candidates for photovoltaic cells [1,2]. For this application, the control of the crystal orientation and morphology of nanowires is quite important because they are crucial parameters for the device performance as well as the doping level and surface conditions.

Copper Zinc Tin Sulfur (CZTS) materials is one of the most promising photovoltaic cell materials to replace CIGS (Cu (In,Ga)S_2 or Cu(In,Ga)Se_2) absorber layer materials. In spite of CIGS the high efficiency nearly 20% [3], however, due to containing expensive rare metals of Indium and Gallium, furthermore, CIGS contain toxic element Se, leading to a photovoltaic cell with environmental disadvantage. Therefore, a research about photovoltaic cell using CZTS as a new PV material has been atracted attention. CZTS has been confirmed as a promising alternative material for low cost absorber layer in photovoltaic cells because of the CZTS containing only the earth-abundant chemical elements of Zn and Sn, and non-toxicity except for the optical-electronic properties similar with CIGS. Furthermore, it has a band gap about 1.4 ~ 1.50 eV [4,5]. By varying the composition of Zinc and Tin in the alloy the band gap can be tuned between the two extreme values, this range of energies is near the optimal energy for absorbing photovoltaic radiation with minimum losses.

CZTS also has a direct band gap which leads to the high absorption coefficient of this material. As a result of this high absorption coefficient and near optimal band gap energy CZTS is a leading material in the field of photovoltaic cells. There are several motivating factors to create photovoltaic cells including thin film photovoltaic cells and nanostructure photovoltaic cells. The film of photovoltaic cell is thin so less material is used than in a regular Si photovoltaic cell. This saves money through lower material costs but risks losing efficiency if the material cannot effectively absorb the incoming sunlight within its thin layer. Although the CZTS thin film have the high absorption coefficient, but the CZTS thin film absorber layer conversion efficiency is still low (11.1%). So the nanostructures absorber layer was focused. We make nanostructure absorber layer application for the photovoltaic cells to improve the conversion efficiency.

In this thesis, the formation techniques and properties of Si and CZTS light absorber layer will be discussed PV applications. The research was discussion and compared regarding the following three categories.

1. *Fabrication of vertical Si nanowires using both Vapor-liquid-solid (VLS) and metal-assisted etching methods.*

We used an AAO as a template to fabricate a Si nanowire arrays by vapor– liquid–solid (VLS) method. Then, we use combination of the self-assembled polystyrene sphere and metal-assisted etching method as a alternation fabrication technique of Si nanowire arrays.

2. *Fabrication and evaluation of CZTS thin films using two-step electrodeposition and non-vacuum CS_2 sulfurization method.*

CuZn/CuSn thin films (precursor) were deposited on Mo-coated Si substrates by two-step electrodeposition method and sulfurization of the precursor was performed in an atmosphere of evaporated CS_2 with Ar as an inert carrier gas. Then, suitable condition of CZTS fabrication was evaluated.

3. *Vertical CZTS nanostructure have been synthesized via both two-steps electroplating method into anodized aluminum oxide template and sputtering method.*

Vertical CZTS nanowire arrays were fabricated by two-step electroplating method into anodized aluminum oxide template. For deposition of CZTS nanowires, anodized aluminum oxide (AAO) was used as atemplate for the growth of the nanowires.

We prepared the vertical CZTS nanocylinder arrays on Si nanowire arrays fabricated with self-assembled polystyrene sphere and metal-assisted etching method as template. Fabricated Si nanowire arrays were used as a template for the sputtering of Mo back electrode and CZTS absorber layers. The optical reflectance of CZTS nanocylinder arrays depending on the length of nanocylinders was investigated.

The technological goal of the thesis is to fabricate vertical Si and CZTS nanostructure to realize cost effective, environmentally friendly and high efficiency Si and CZTS photovoltaic cell.

References of chapter 2

[1] B. Tian, X. Zheng, T. J. Kempa, Y. Fang, N. Yu, G. Yu, J. Huang, and C. M. Lieber: Nature 449 (2007) 885.

[2] B. Wang and P. W. Lue: Nanotechnology 23 (2012) 194003.

[3] I. Repins, M. Contreras, B. Egaas, C. DeHart, J. Scharf, C. Perkins, et al: Res Appl. 16 (2008) 235.

[4] K. Ito, T. Nakazawa: Jpn J Appl Phys. 27 (1988) 2094-7.

[5] T. Tanaka, T. Nagatomo, D. Kawasaki, M. Nishio, Q. Guo, A. Wakahara, A. Yoshida, H. Ogawa: J Phys Chem Solids. 66 (2005) 1978-81.

CHAPTER 3

CHARACTERIZATION METHODS: PRINCIPLES AND EQUIPMENTS

Several methods have been used to characterize structure and properties of the CZTS thin films and nanostructures in this study. For structural characterization, the techniques such as X-ray diffraction (XRD), Raman scattering spectroscopy and transmission electron microscopy (TEM) were employed. The morphology analyses and compositional characterization were accomplished by scanning electron microscopy (SEM) and X-ray photoelectron spectroscopy (XPS), including energy-dispersive X-ray analysis (EDX), respectively. XPS and EDX were additionally utilized to examine the composition of the films. The optical and electrical properties of the films were determined by UV-Vis spectroscopy and Photoluminescence (PL) spectroscopy. In this chapter, the main principles of these techniques are briefly described.

3.1 Structural characterization methods (XRD, Raman, and TEM)

3.1.1 X-ray Diffraction

X-ray diffraction is a powerful non-destructive method for material characterization, by which the crystal structure, orientation, and grain size can be determined. When X-rays impinge on a crystal, the individual atoms act as secondary radiation emitters and cause interference. Constructive interferences give the diffraction peaks according to Bragg's law,

$$2d\ \sin\theta = n\lambda, \quad (n=1,2,3\ldots\ldots) \tag{4.1}$$

which relates the distance between a set of planes, d, in a crystal and the angle, θ, at which these planes will diffract X-rays of a particular wavelength, λ.

Fig. 3.1 shows the schematic of a Bragg Reflection and a standard Bragg-Brentano powder diffractometer. In such a powder diffractometer, the sample stage and detector can only rotate in the same plane, along the same axis perpendicular to the sample stage. In θ-2θ scan, the reflections from the planes parallel to the substrate surface are detected. This allows determining the orientation along the growth direction of an epitaxial layer or preferentially oriented polycrystalline film with respect to the substrate. In addition, the full width at half maximum (FWHM) of the peak, $\Delta(2\theta)$, is a measure of the size, b, of the grains in a polycrystalline film in an epitaxial layer, as described by Scherrer's formula [1]:

$$b=0.89\lambda/\Delta(2\theta)\cos(\theta), \tag{4.2}$$

where θ is the Bragg angle and λ the X-ray wavelength.

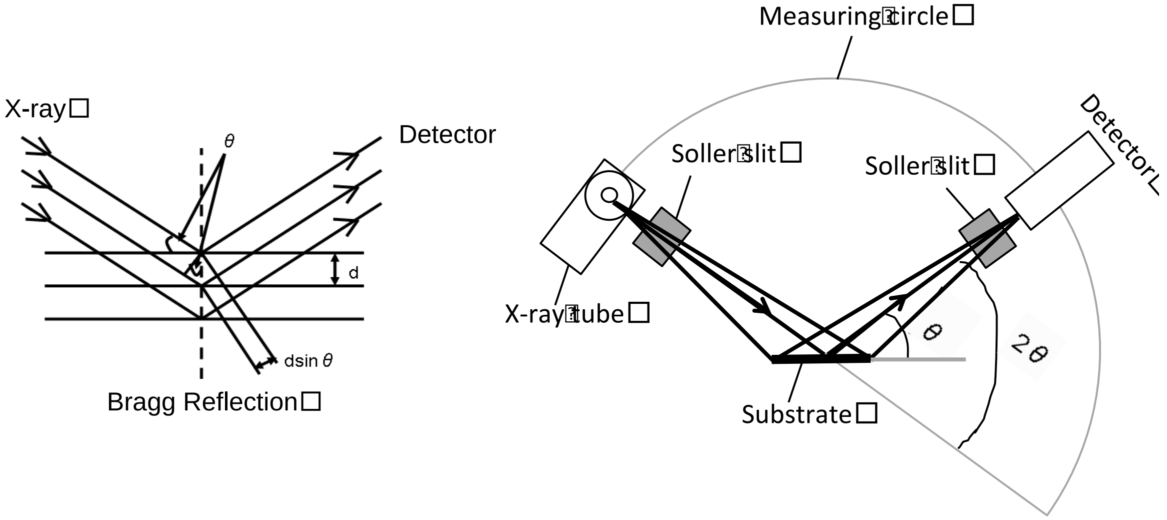

Fig. 3.1 The schematic of a Bragg Reflection and a standard Bragg-Brentano powder diffractometer.

3.1.2 Raman Scattering Spectra

Raman spectroscopy is a spectroscopic technique used to study vibrational, rotational, and other low-frequency modes in a system. It relies on Raman scattering, usually from a laser, the laser light interacts with molecular vibrations in the system, resulting in the energy of the laser photons being shifted up or down. The shift in energy gives information about the vibrational modes in the system. Raman spectroscopy can be used to observe low frequency excitations of the solid materials. So using Raman spectroscopy measurement method we can find the crystallographic orientation of a sample.

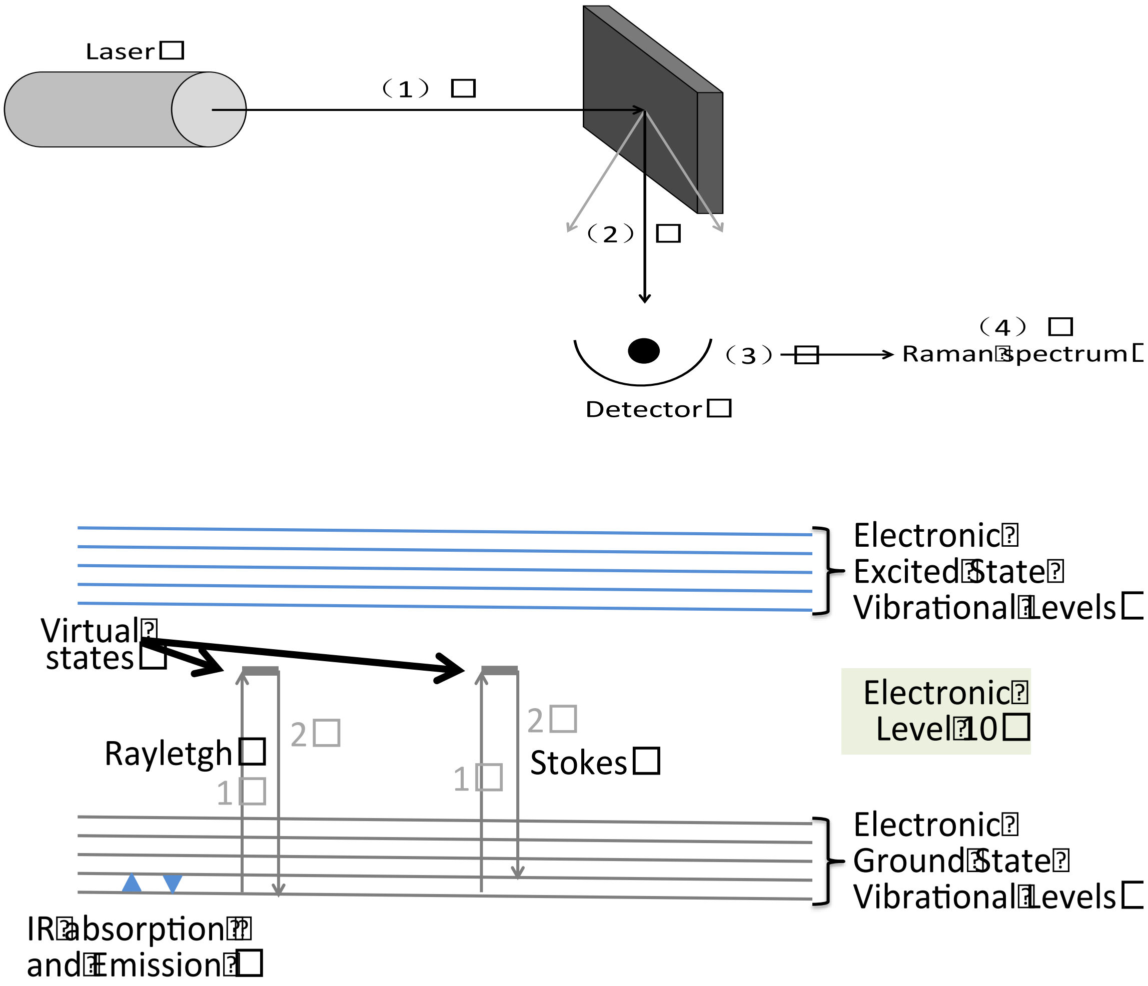

Fig. 3.2 The working principle of Raman spectroscopy

Fig. 3.2 shows the working principle of Raman spectroscopy. First, Laser light excites the sample shows in number (1). Then, this light is scattered in all directions shows in number (2). Some of this scattered light is directed to the detector, which records the Raman spectrum shows in number (3). Spectrum (4) shows light at the original laser frequency and the Raman spectral features unique to the sample. Following figure is the energy-level diagram, this diagram showing the states involved in Raman signal. The line thickness is roughly proportional to the signal strength from the different transitions.

In this thesis, Raman spectroscopy was performed owing to difficulty of peak separation of CZTS from impurity phase of ZnS, Cu_2SnS_3 (CTS) by XRD measurements.

3.1.3 Transmission Electron Microscopy

Transmission electron microscopy is a versatile tool capable of characterizing the internal structure of a wide range of materials [2]. TEM characterization enables not only the direct imaging of the microstructure, but also the identification of the phases present in the specimen by either electron diffraction or spectroscopic chemical analysis. The results obtained from a typical TEM characterization offers a better understanding of the relation between the microstructure and properties of the materials.

There are various operation modes of the electron microscope. The bright field (BF) mode is usually used to image grains and defect structures within the specimen. It can also reveal secondary phases such as precipitates or inclusions. Similar in purpose to the BF technique, the dark field (DF) imaging mode uses the specific Bragg diffracted electrons to image the region from which they originated. The DF mode enables the connection between the crystallographic information and specific regions or phases in the sample. The principal function of the electron diffraction technique is to determine the crystallographic structure of the material being analyzed. By placing an aperture in the image plane, then projecting the diffraction pattern of that image onto the recording plate, the HAADF is obtained.

For more detailed description of TEM techniques and practical applications in material research refer to [2-5].

3.2 Morphology and composition characterization methods (SEM, EDX, XPS)

3.2.1 Secondary Electron Microscopy

A secondary electron microscope (SEM) operates through the use of a focused electron beam in a high vacuum chamber. This excitation can occur through field emission. Following the generation of the electron beam the electrons are accelerated to the desired energy by high voltage and then focused through various electron optic elements to produce a beam with the desired beam size and shape. This beam can then be adjusted to a desired position by potential plates in the beam path. The beam can be focused to a very high degree resulting in nanometer scale resolution.

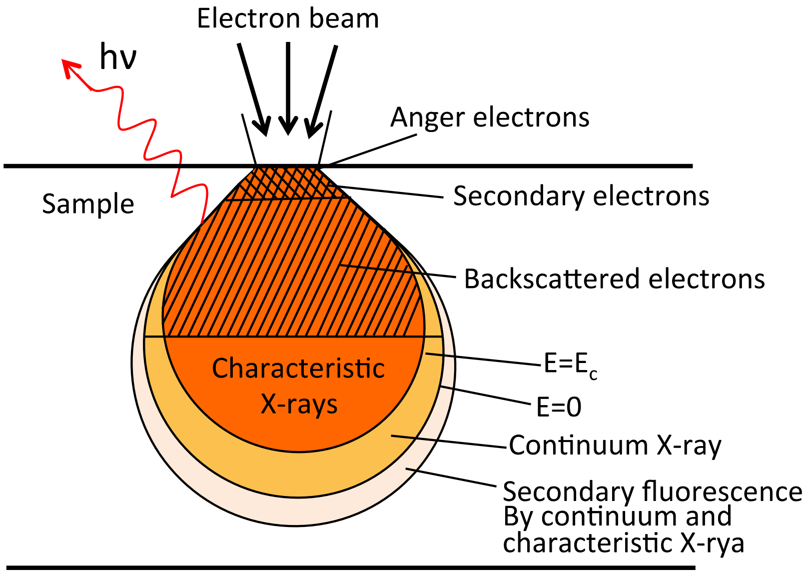

Figure 3.3 Electron scattering processes generated by SEM electron beam illumination.

The electron beam reaches the sample, a series of scattering events occur first with the incident electrons and the sample, and then later with the secondary electrons. This process is illustrated in Figure 3.3. The imaging function of a secondary electron microscope is accomplished by detecting the intensity of the secondary electrons emitted from the sample at each point on the sample surface, as the electron beam is restored across the surface. These electrons, as shown in Figure 3.3, can only escape from the sample surface from the top ~ 50 nm of the sample. This makes these electrons sensitive to the surface features of a sample. The contrast seen in the image is a result of both the topography of the surface and changes in the work function of the surface.

3.2.2 Energy Dispersive X-ray

Energy dispersive X-ray analysis (EDX) is detection and measure of the characteristic X-rays enables elemental analysis. EDX provides rapid qualitative, or with adequate standards, quantitative analysis of elemental composition within a sampling depth of 1-2 microns. X-rays may also be used to form maps or line profiles, showing the elemental distribution in a sample surface. General information on working principles of SEM and its versatile applications in materials science can be found for instance in [6-8].

3.2.3 X-ray Photoelectron Spectroscopy (XPS)

X-ray photoelectron spectroscopy (XPS), known as electron spectroscopy for chemical analysis (ESCA), is extreme surface sensitive methods for chemical and electronic characterization of materials. Irradiating a sample in vacuum with X-rays or ultraviolet radiation and analyzing the energy of the detected electrons accomplish surface analysis by XPS.

The spectrum is obtained as a plot of the number of detected electrons per energy interval versus their kinetic energy. Since each element has a unique set of binding energies, XPS can be used to identify the elements in the surface qualitatively referring to the peak positions, and determine quantitatively the concentration of each element.

3.3 Optical Characterization Methods (UV-Vis, PL)

3.3.1 UV-Vis Reflection Spectroscopy

The optical properties of the ilms were characterized by UV-Vis reflection spectrum measurements. The reflection spectra were recorded in the wavelength range of 300-900 nm at room temperature. According to the reflection spectra, the absorption coefficient α of the films was evaluated with the expression

$$T=e^{-\alpha t} \tag{4.3}$$

which neglects the surface and multiple reflection effects. Here T is the transmission coefficient and t the film thickness. Following the usual theoretical analysis [9], the energy dependent absorption coefficient $\alpha(hv)$ can be expressed by the relation for the allowed direct transition as

$$\alpha(hv)=A(hv-E)^{1/2} \tag{4.4}$$

where A is a constant, hv the photon energy, and E refers to the direct band edge. By extrapolating along the linear portion of theα^2 versus hv curve to the hv axis, the direct bandgaps of the films, represented by the intercept at the hv axis, were deduced.

3.3.2 Photoluminescence Spectroscopy

This technique involves probing the semiconducting sample with an electron beam and measuring the emitted light. PL gives information regarding the band structure of the sample including the band gap and defect levels within the band gap. The basic physics are similar for the emission processes. The excitation is now accomplished when a valence band or defect state electron absorbs an incident photon and is excited into the conduction band or some other higher energy state.

In this work, a Cd-He laser was used to excite CZTS samples for measurement. The PL setup consisted of a band pass filter to remove undesirable laser emission lines and lenses to focus the incident light onto the sample. The emitted light was collected by a secondary optical path and focused onto an Oriel diffraction grating monochromator. The same liquid nitrogen cooled discussed in the previous section detected the signal and the intensity was then measured to give the value of the signal strength.

References of chapter 3

[1] B. E. Warren, X-ray Diffraction: Addison-Wesley Publishing Company, 1969, p. 253.

[2] D. B. Wiliams and C. B. Carter, Transmission electron microscopy: a textbook for materials science. New York: Plenum press, 1996.

[3] G. Thomas, Transmission Electron Microscopy of Metals. New York: John Wiley and Sons Inc., 1962.

[4] J. C. H. Spence, Experimental High Resolution Electron Microscopy, Monographs on the Physics and Chemistry of Materials. Oxford: Clarendon Press, 1981.

[5] J. M. Gibson, High Resolution Transmission Electron Microscopy, MRS Bull. (March), 27, 1991.

[6] O. C. Wells, Scanning Electron Microscopy. N. Y.: McGraw-Hill Book Company, 1974.

[7] D. E. Newbury, D. C. Joy, P. Echlin, C. E. Fiori, and J. I. Goldstein, Advanced Scanning Electron Microscopy and X-Ray Microscopy. New York: Plenum Press, 1986.

[8] I. M. Watt, Principles and Practice of Electron Microscopy. Cambridge University Press,1985.

[9] J. I. Pankove, Optical processes in semiconductors. New Jersey: Prentice-Hall, Englewood Cliffs, 1971.

CHAPTER 4

FABRICATION OF VERTICAL SI NANOWIRE ARRAYS

4.1 Vapor-liquid-solid growth of Si nanowires using AAO template

The control of the crystal orientation and diameter of vertically grown epitaxial Si nanowires was demonstrated using a combination of a vapor– liquid–solid (VLS) growth technique and the use of an anodic aluminum oxide (AAO) template on a single-crystal Si substrate.

4.1.1 Anodic aluminum oxide (AAO)

Anodic aluminum oxide (AAO) is known to have ordered honeycomb nanopore arrays, perpendicular to the substrate, the diameter of which can be controlled from a few nanometers to several hundred nanometers depending on the anodic voltage and acid species used for anodization. Voltage dependence of the pore array formation is shown in Fig.4.1. The oxalic acid concentration is 0.15 M and the temperature is 5 ^{O}C. The pore and cell diameters monotonically increased with increasing voltage, as previously reported [1,2]. In order to explain the effect of self-organization, the situation during steady state pore growth has to be considered (Fig.4.2). Pores grow perpendicular to the surface with equilibrium of field-enhanced oxide dissolution at the oxide/ electrolyte interface and oxide growth at the metal/oxide interface. While the latter is due to the migration of oxygen containing ions (O^{2-}/OH^{-}) from the electrolyte through the oxide layer at the pore bottom, Al^{3+} ions, which simultaneously drift through the oxide layer, are ejected into the solution at the oxide/electrolyte interface. The fact that Al^{3+} ions are lost to the electrolyte has been shown to be a prerequisite for porous oxide growth, whereas Al^{3+} ions, which reach the oxide/electrolyte interface, contribute to oxide formation in the case of barrier oxide growth. The atomic density of aluminum in alumina is by a factor of two lower than in metallic aluminum. A possible origin of forces between neighboring pores is therefore the mechanical stress, which is associated with the expansion during oxide formation at the metal/oxide interface. Since the oxidation takes place at the entire pore bottom simultaneously, the material can only expand in the vertical direction, so that the existing pore walls are pushed upwards [3].

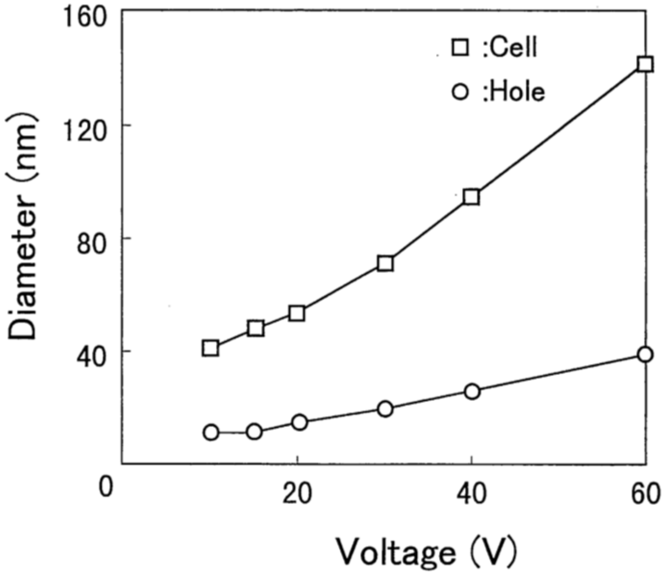

Fig.4.1 Average diameter of the pores and cells as a function of the voltage of anodic oxidation. [2]

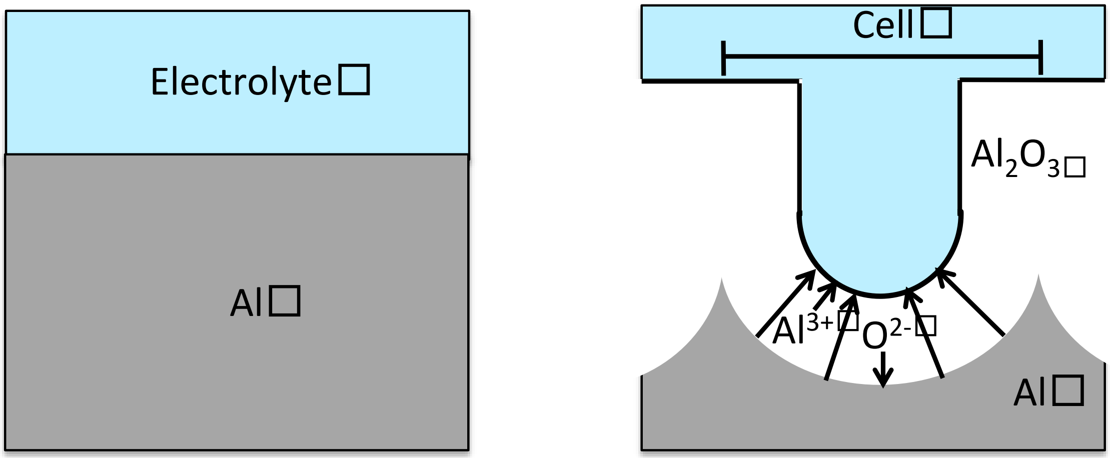

Fig.4.2 Growth mechanism of AAO pores.

4.1.2 Reduction of pich of AAO nanohole arrays

AAO has been used as a template for the fabrication of various nanostructures since it has many advantages, such as small nanopore diameter, high packing density, and very low cost compared with conventional lithographic techniques [4-12].

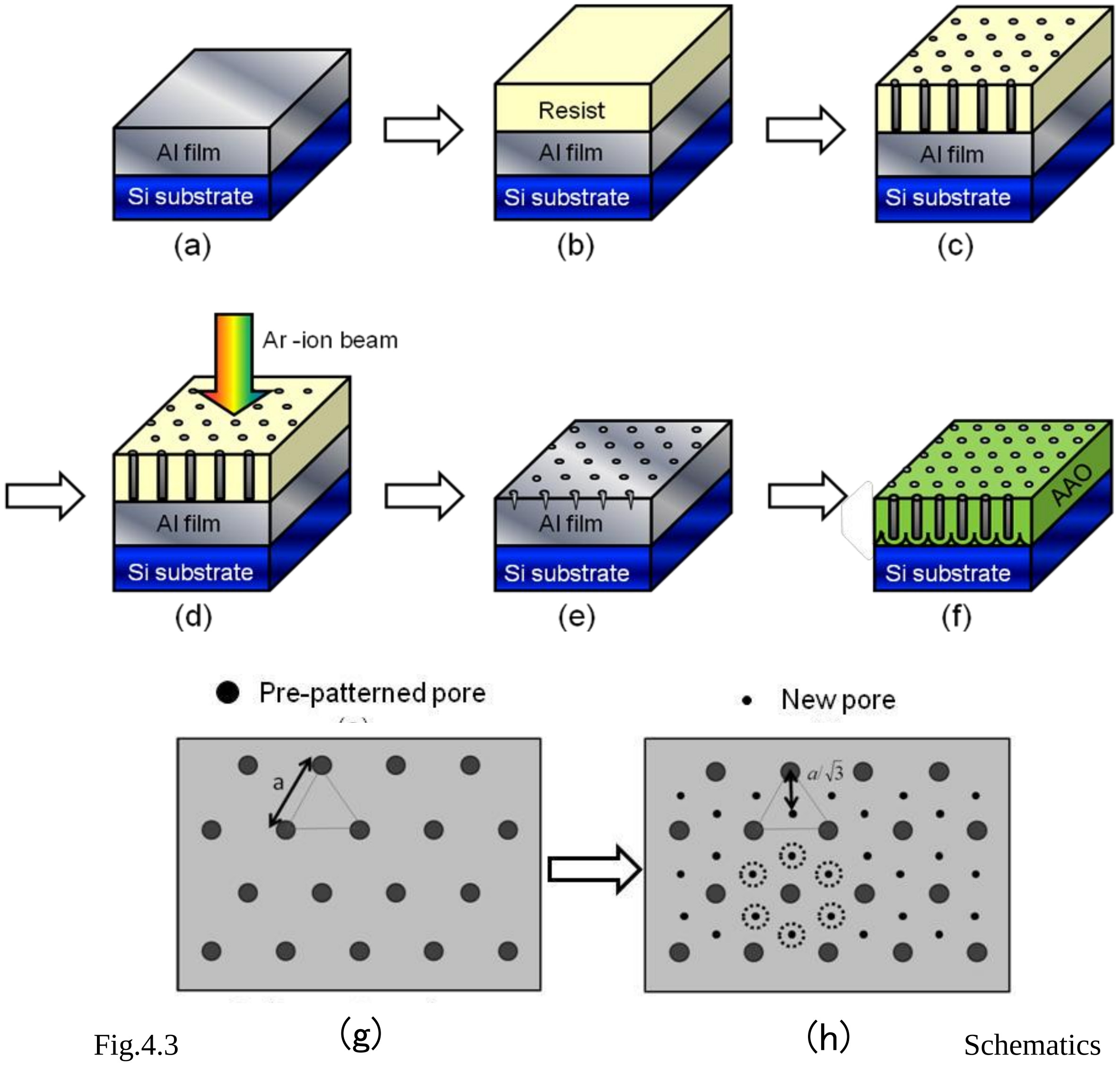

Fig.4.3 Schematics of the sample preparation (a) Al film is sputtered on Si substrate. (b) Resist film is fabricated using spin-coating method. (c) The periodically holes is fabricated in resist film by electron beam lithography. (d) Formation of pits on Al film by IBE. (e) Removal the EBL resist mask. (f) Anodic oxidation of Al. (g) The top-view of (e), dots indicate indentations having an order triangular array. (h) The top-view of (f), the smaller dots indicate position of new pores formed by anodization.

However, it is known that the ordered AAO pore arrays can be obtained by several appropriate growth conditions, and the inter-pore distances of ordered AAO pore arrays are limited. Moreover, preparation of fine pitch arrays is getting more difficult, especially below 100 nm. We tried to prepare AAO on Si substrate with an inter-pore distance of 60 nm using a guided self-organization method.

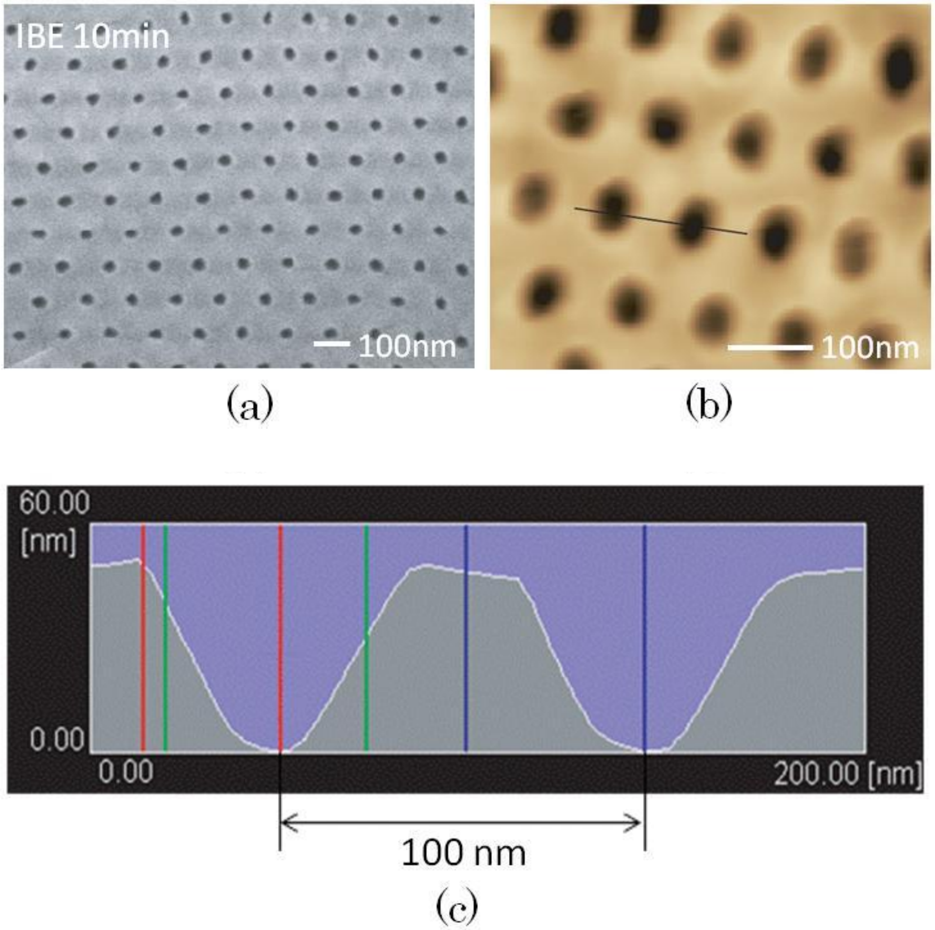

Fig.4.4. SEM and AFM measurements of the ordered nanopore arrays after prepatterning on Al surface. (a) Nanopores of prepatterned Al surface were observed by SEM after ion beam etching at 10min, the interpore distance of nanopore was approximately 100nm. (b) Nanopores of prepatterned Al surface were observed by AFM. (c) Line scan of AFM height image shown in (b).

Fig.4.3 (a)-(f) shows the described schematically of experimental procedure. At first, 500 nm thick Al film was deposited on treated Si substrate (Si was treated with HF solution) by sputtering using Al target (99.999%) as shown in Fig.4.3 (a). Then, about 100 nm thickness resist film was fabricated by spincoating method (300 rpm 5 sec, 2000 rpm 180 sec) using ZEP520A resist (use Anisol diluted into 2:3) as shown in Fig.4.3 (b), the pre-bake was carried out on 180 ^{O}C hot plate at 180 sec after spincoating. Subsequently, the triangular lattice of pits with a pitch of 100 nm was prepared by electron beam lithography (EBL) on sputtered Al film on Si substrate as shown in Fig.4.3 (c). 75 kV acceleration voltage electron beam selectively etches off regions of the positive resist from the surface (ELIONIX ELS-7700, JAPAN). IBE was carried out at 23 ^{O}C with 180 sec using ZED-N50 developing solution.

Then, using pits pattern as a mask for Ar ion beam etching (IBE) (Fig.4.3 (d)), IBE was carried out in the different duration of IBE under the conditions of beam voltage with 150 V and accelerator voltage with 700 V in the 2.5×10^{-2} Pa chamber. (RIB-E, TYD, JAPAN) we transferred the triangular lattice pattern to the Al surface as shown in Fig.4.3 (e). For Ar IBE, acceleration voltage was kept constant at 700 V, and etching time was changed from 5 min to 10 min. After that, the EBL resist mask was completely removed from Al surface by selective etching with 10 min in acetone. The Al surface of 10 min IBE sample was observed by the top-view of SEM and AFM as shown in Fig.4.4 (a) and (b), respectively. Fig.4.4 (c) shows the AFM Line scan of nanopores of prepatterned Al surface from Fig.4.4 (b). According to AFM Line scan and top view of SEM image we can know that the interpore distance was approximately 100 nm, the depth was 50 nm, and the arrangement of pits was perfectly ordered as triangular lattice without any defects and dislocations. Thus, the periodically prepatterned Al surface was obtained. Then, prepatterned Al surface was anodized at various voltages between 24 to 30 V in 0.3 M sulfuric acid electrolytes as shown in Fig.4.3 (f). Fig.4.3 (g) and (h) shows the surface of the Fig.4.3 (e) and (f), respectively. The pits having an ordered triangular array of nanopores with a pitch of 100 nm on Al surface shows in Fig.4.3 (g), and the Al is anodized after prepattern, the small dots were formed at the center of each triangle of the initial pits, then $1/\sqrt{3}$ reduction of interpore distance is achieved at an adequate anodic voltage. The surface morphology of Al and AAO pore arrays were observed by scanning electron microscope (SEM) and AFM. The regularity of AAO pores was quantitatively evaluated by the fast Fourier transforms (FFT) of the SEM images.

Fig.4.5 shows top-view SEM images of the AAO pore arrays using patterned Al films, which was anodized at various voltages from 24 to 30 V. It can be observed that the interpore distance between the lager AAO pores indicated with black circles was 100 nm, which corresponds to the pitch of the IBE mask. Therefore, these pores were grown at the prepatterned positions on the Al surface. The smaller pores indicated with dashed circles were newly created pores located at the center of hexagon of prepatterned pores, which worked as the guide to determine a position of nucleation sites of new pores. The anodic voltage dependence of pore arrangement is shown in Fig.4.5 (a)-(c). Although the arrangement of the new AAO pores was not a perfect triangular lattice, we found that 28 V is an appropriate voltage to realize the $1/\sqrt{3}$ reduction of the pitch for the array prepatterned with 100 nm pitch in these conditions. Some prepatterned AAO pores are elongated with two-fold depression at a single location, as indicated for example by the arrows in Fig.4.5 (a) and (c). It seems that the oversized pits for the guided self-organization cause the dislocation and defect of the triangular AAO pore arrays, and the size and depth of pits would be important.

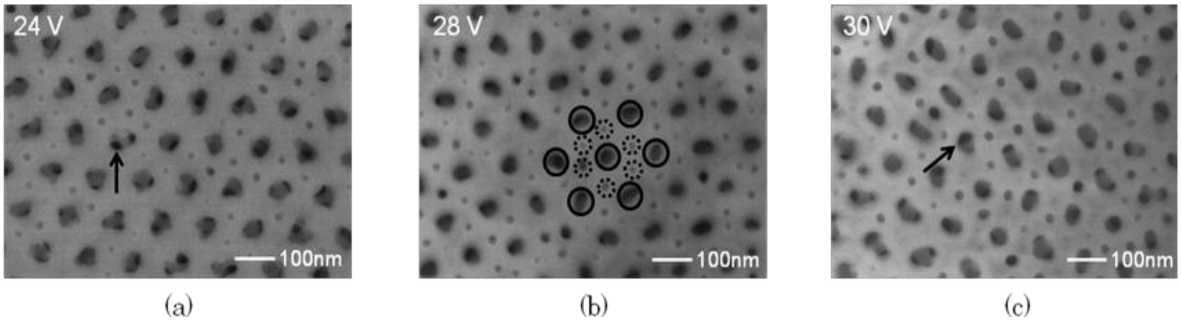

Fig.4.5. SEM image of the surface of AAO after anodic oxidation of aluminum for various anodization voltages. (a) 24V anodic voltage. (b) 28V anodic voltage. (c) 30V anodic voltage.

Fig.4.6 (a)-(c) shows top-view SEM images of AAO pore arrays using guided self-organization method with different duration of IBE for prepatterning. We analyzed the SEM images by two-dimensional FFT to evaluate the IBE duration dependence of the nanohole regularity as shown in Fig.4.6 (d)-(f). The triangular arrays of spots were clearly observed in 7.5 and 10 min of IBE etching samples while only fuzzy spots were observed in the 5 min sample. The cross section of the FFT intensity distribution along the red line is shown in the Fig.4.6 (g)-(i). The regularity of the nanohole arrangement is well represented by the intensity of order spots (indicated with arrows in Fig.4.6 (h) and (i)). Hence, we chose a spatial order parameter, I/W (the first spots intensity I divided by its full width at half maximum width (FWHM)). In the FFT cross-sections, two series of peaks appear at increasing distances from the center (first spot and second spot are shown in Fig.4.6 (h) and Fig.4.6 (i), respectively). The periodic function of strcture such as nanohole arrays in real space corresponds to the reciprocal distance of ordered spot in FFT image. Therefore, first ordered spots in Fig.4.6 (i) correspond to the original prepattered lattice (~100 nm pitch), and the second ordered spots are secondary lattice formed by anodization (~60 nm pitch), respectiverly.

The regularity ratio I/w of the prepatterned lattice peak increases from Fig.4.6 (g) to Fig.4.6 (i), as expected, since longer IBE patterning time means better defined starting pattern. However, the peak arising at higher spatial frequency (i.e. lower pitch) due to anodization, Table.4.1 shows regularity as a function of the IBE duration; has the highest regularity ratio about 7.3 for the intermediate case of Fig.4.6 (h) 7.5 min IBE, and it seems that the pits of 5 min IBE was not enough for the guide of new pores. These results suggested that 7.5 min IBE was the appropriate condition for guided self-organization of interpore distance of 60 nm, while the 10 min IBE caused over-etching.

Table.4.1: Ion beam etching duration dependence of nanohole regularity

IBE duration [min]	5	7.5	10
Regularity (I/W)	2.4±0.2	7.3±0.2	4.1±0.2

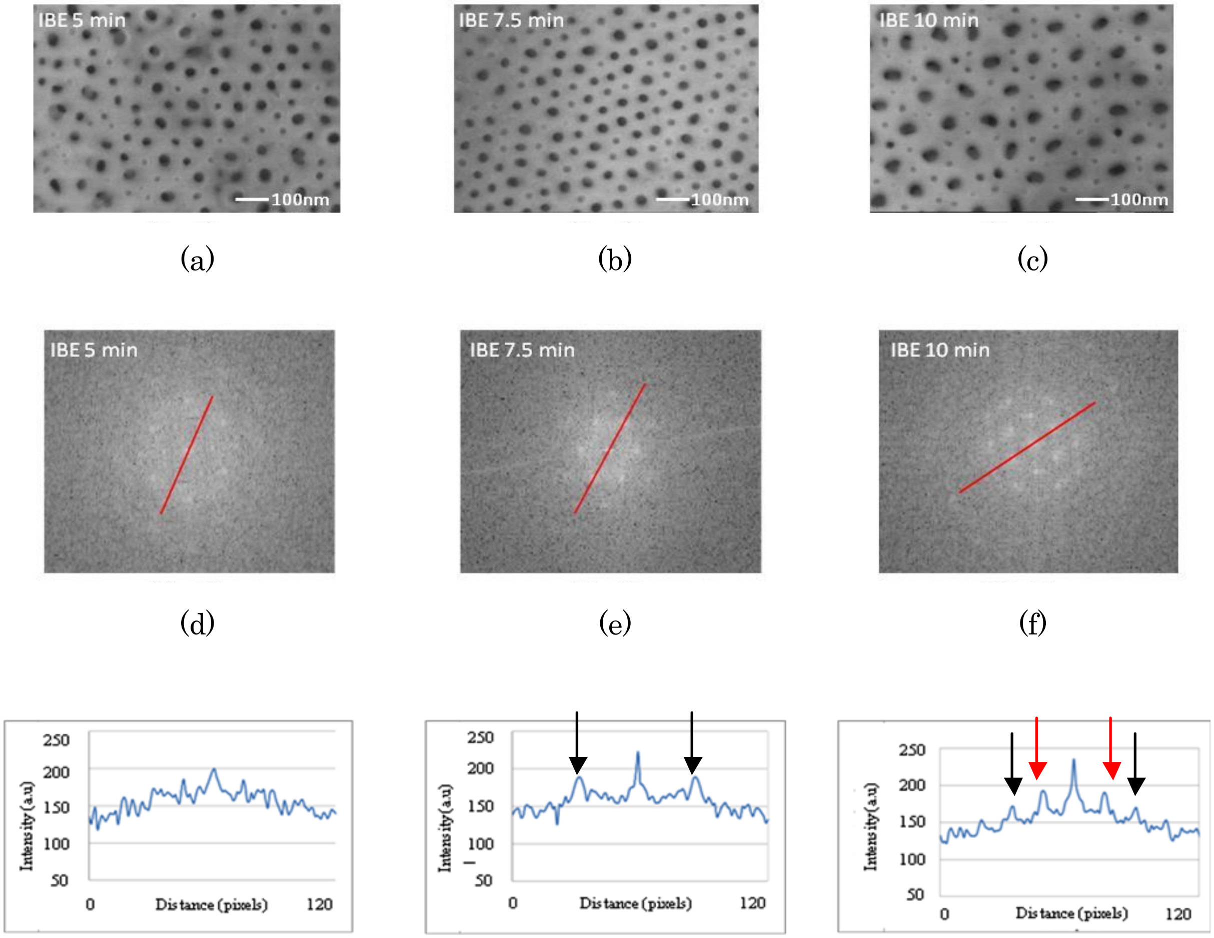

(a) (b) (c)

(d) (e) (f)

Fig.4.6. (g) (h) (i) SEM micrographs of the surface of AAO after anodic oxidation of aluminum at 28V for various ion beam-etching times. (a)-(c) The top-view SEM images of surface of the AAO membrane just after anodic oxidation at 28V with 5min, 7.5min, 10min IBE times. (d)-(f) Two-dimensional FFT images for the nanopore arrangements shown in Fig.4 (a)-(c). (g)-(i) are cross-section of the FFT intensity distribution along the red line in Fig.4 (d)-(f). The red and black allows in Fig(d)-(f) indicate first- and second-ordered sports of nanohole arrays.

The ordered nanopore arrays with the interpore distance of 60 nm on Si substrate were successfully prepared using 100 nm pitch of prepatterned Al films with IBE and guided self-organizing of AAO. It turned out that there was an appropriate IBE condition and anodization voltage for realizing ordered AAO nanopore arrays in this method. This method allows further reduction of AAO interpore distance, and it would be possible to realize triangular pore arrays with smaller interpore distance beyond the size limitation of the lithographic technique.

In this thesis, AAO has been used as a template for the fabrication of Si and CZTS nanostructures since it has many advantages, such as small nanopore diameter, vertical grown and high packing density.

4.1.3 Formation of AAO on Si substrate

Fig.4.7 shows electro chemical cell for formation of AAO on Si substrate. First, Al films were deposited by sputtering on each Si substrates. Pressing the Si substrate to a Cu block from the backside of the sample formed an electrical contact for the anodization of the Al film. The temperature of the Cu block was maintained at 5 ^{O}C. Therefore, we prepared AAO template using anodization of the Al film, which was carried out in an electrolyte based on oxalic acid (0.3M $H_2C_2O_4$ with deionized water) at 40V by a two-step anodization technique [13].

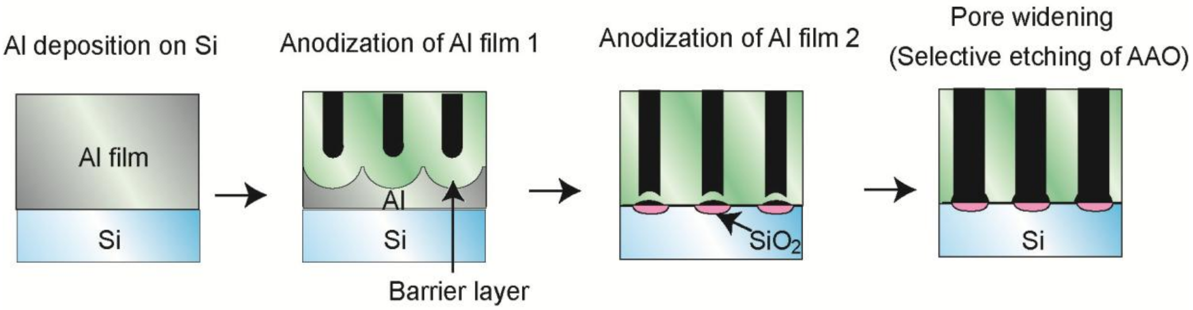

Fig.4.7 Electro chemical cell for anodization of Al film on Si substrate.

The first anodization was stopped when the thickness of the rest of the Al film on the Si substrate reached about 500 nm. After the selective etching of the first AAO film by wet chemical etching (30 min, 60 ^{O}C, mixture of 6wt % phosphoric acid and 1.8 wt % chromic acid), a second anodization was performed until the entire Al film changed into AAO. Then, we slightly etched the aluminum oxide using dilute phosphoric acid (20 min, 30 ^{O}C, 5%). The last one of the Fig.4.7 shows typical AAO pore arrays on a Si substrate. The bottom of AAO pores was slightly widened compared with the middle part of the pores owing to the mechanism of the anodization on the Si substrate discussed elsewhere [14].

4.1.4 Vapor-liquid-solid (VLS)

The vapor–liquid–solid (VLS) method is a mechanism for the growth of one-dimensional structures, such as nanowires, from chemical vapor deposition. The growth of a crystal through direct adsorption of a gas phase on to a solid surface is generally very slow without catalysts. The process is illustrated in Fig. 4.8 for the selective growth of a silicon crystal.

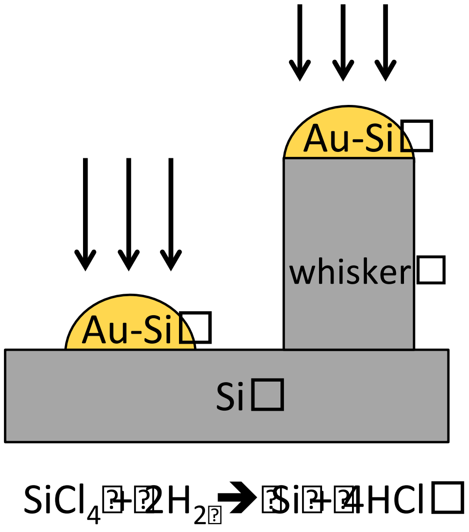

Fig.4.8 Schematic illustration of Si whisker growth from the reaction of $SiCl_4$ and H_2 vapor phases using VLS method

First, Si atoms deposition is directly deposited on a solid substrate in a vapor-solid system. There are two kind of deposition mechanism existing during CVD process with catalysis. One is deposition mechanism occurred without catalyst. In this case, therefore, growth rate of Si is very slow. The second process, which is the VLS mechanism with catalase, occurs in two steps as has been described. First. There is deposition from the vapor directly on a liquid solution in a vapor-liquid system. The second and subsequent step, occurring in a liquid-solid system, is precipitation from the supersaturated liquid solution at the liquid-solid interface.

4.1.5 Sample preparation

Fig.4.9 shows a schematic drawing of the sample preparation. First, the AAO templates were formed on Si substrate; then, the Si oxide at the bottom of nanopores hinders the epitaxial growth of buried material in an AAO template. Therefore, the HF treatment of the AAO template was necessary to remove the oxide layer. The annealing of the AAO template was carried out prior to the HF treatment to prevent the dissolution of the template. The AAO templates were annealed in Ar gas (3×10^{-3} Torr, 99.995%, back-ground pressure 1×10^{-6} Torr) for 3 h at 900 ^{O}C.

We dipped the AAO templates in dilute HF solution (15min, 1%, at room temperature), and then the Si oxide layer at the bottom of the pore was etched away. Subsequently, the AAO templates were immersed in a mixture of 20 ml of 0.02 M $KAuCl_4$ and 18 ml of 49% HF for the electroless plating of Au. The electroless deposition of metals from an electrolyte containing HF could be explained by galvanic displacement reactions [15].

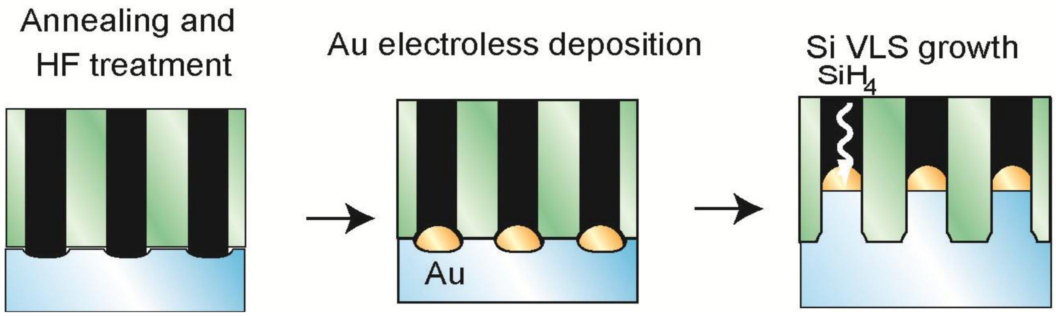

Fig. 4.9 Schematic drawing of sample preparation procedure of vertical epitaxial Si nanowire using AAO template and VLS method (a) AAO template on Si substrate (b) Au electroless deposition on Si surface in AAO pore (c) VLS growth of Si nanowire using Au particles as catalyst in AAO pores. [16]

In our system, exchanging electrons through the Si substrate, the reduction of metal ions as a cathodic process and the oxidation of Si atoms as an anodic process occur simultaneously at the Si surface. As a result, Au particles are deposited at the bottom of AAO pores. The samples were transferred into a low-pressure chemical vapor deposition (LP-CVD) system. The growth of Si nanowires was carried out at a temperature of 480 ^{O}C in 2.0 Torr SiH_4 /He gas with a partial pressure of SiH_4 of 6.6×10^{-2} Torr.

4.1.6 Results

(VLS growth of ordered Si nanowire arrays using AAO template)

Fig.4.10 shows a cross-sectional TEM image of the vertically aligned Si nanowire arrays in an AAO template anodized with 40 V on a Si (100) substrate. Au particles were observed at the top of nanowires. The average interpore distance and diameter of the AAO template were about 100 and 65 nm respectively, and the thickness of the TEM specimens was less than 80 nm. Therefore, only one nanowire was observed in these TEM images without any overlapping. The density of nanowire arrays using an AAO template with an anodization voltage of 40 V was about 100um^{-2}. The enlarged view of the bottom of the nanowire indicated as a box in Fig. 2 is shown in our previous paper [17]. These nanowires were epitaxially grown on a Si(100) substrate and the growth direction was [100].

We have demonstrated the control of the growth direction, crystal orientation, and diameter of Si nanowires epitaxial grown on Si substrates using an AAO template and catalytic VLS growth with silane gas. The growth of the Si nanowires was guided by the AAO pores into the vertical direction of the surface of the substrate, and the diameter of the wire fits the pore size. The epitaxial Si[100], nanowires were obtained on the Si(100) substrates. These results indicated that the crystal orientation of the nanowire could be selected by choosing a Si substrate cut in the desired orientation under the AAO template. Moreover, modifying anodic voltage during AAO preparation controlled the pore diameter of the nanowire. This method allows independent control of the diameter and crystal orientation of the vertically grown epitaxial nanowires.

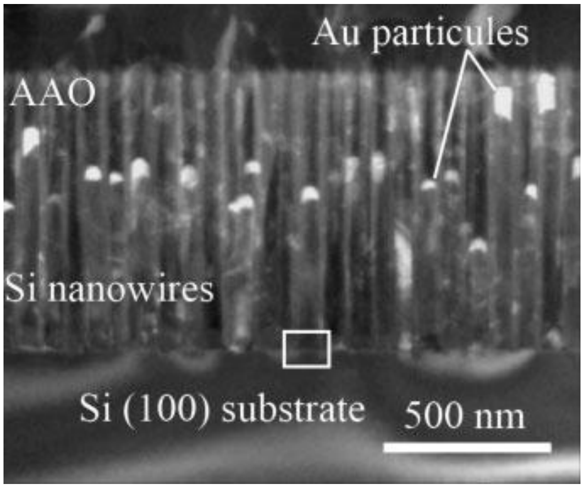

Fig. 4.10 Cross-sectional TEM image of Si nanowire arrays in AAO template, the box at the bottom of the nanowire indicates the area observed by HR-TEM.

4.2 Self-assembled polystyrene sphere and metal-assisted etching method

Self-assembled polystyrene sphere made of Si nanowires have been applied to generate various functional nanostructures.

4.2.1 Sample preparation

We present the application of a low-cost self-assembled polystyrene sphere method to generate high aspect ratio silicon nanowires by high-density plasma reactive plasma ion etching. The diameter and interwire distance of these nanowires were controlled using polystyrene nanospheres with various sizes and etching these spheres with oxygen plasma to tailor the diameter of the nanosphere.” Since these nanospheres are densely packed with separation, their packing density drastically affects the flow of reactive ion etchants and effluent ion species during the etching process. Thus, both the separation of etched “resists” and the etch time control the etch rates of silicon.

The overall fabrication process is schematically depicted in Fig.4.11. First, the ordered monolayer of polystyrene (PS) spheres arrays on SiO_2 layer prepared by self-assemble method. Subsequently, oxygen plasma ashing process was used to reduce the diameter of the PS spheres. In the next step, an Au film was sputtered onto the silicon substrate with PS array as a catalyst for the following metal assisted etching step. Owing to the PS monolayer mask, an Au film with a hexagonal array of holes was formed. The diameters of the holes match that of the diameter reduced PS spheres. An etching step was conducted in a mixture of deionized water, HF, and H_2O_2. Then, the Au film worked as a catalyst for the etching of silicon beneath itself. During the etching process, the “walls” of the honeycomb structure between PS spheres were gradually etched away and the remained silicon forms a nanowire array. Finally, the Au film was dissolved and the PS spheres are removed by oxygen plasma again.

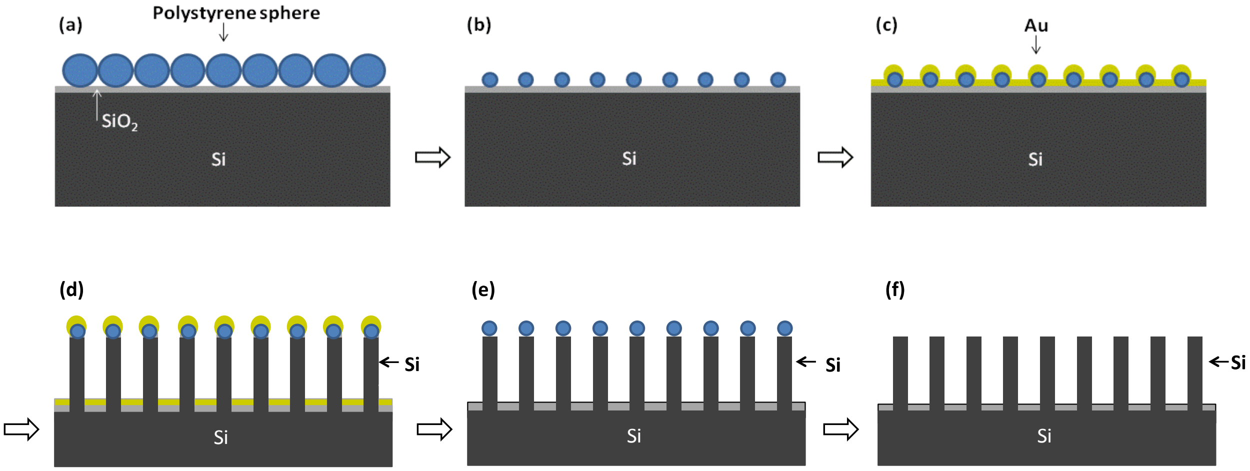

Fig. 4.11 Schematic depiction of the fabrication process
(a) Coat a polystyrene spheres on substrates (b) tailor the size of the polystyrene spheres by oxygen plasma etching. (c) Deposition of Au films by sputtering method (d) Etch the exposed Si areas by deep reactive ion etching (e) removed the Au films (f) the PS spheres are removed by oxygen plasma

4.2.2 Results

Fig. 4.12 shows the low-magnification scanning electron microscopy (SEM) images of the PS spheres arrays on large area of silicon substrate. Disturbances in the periodic arrangement of PS spheres, such as point defects and grain boundaries, are also observed in the SEM image. These defects would be avoided by precise control of the self-assembly process. Fig. 4.12(b) is high-magnification SEM image of PS sphere arrays. The ordered PS arrays with diameter of 500 nm without overlapping can be observed.

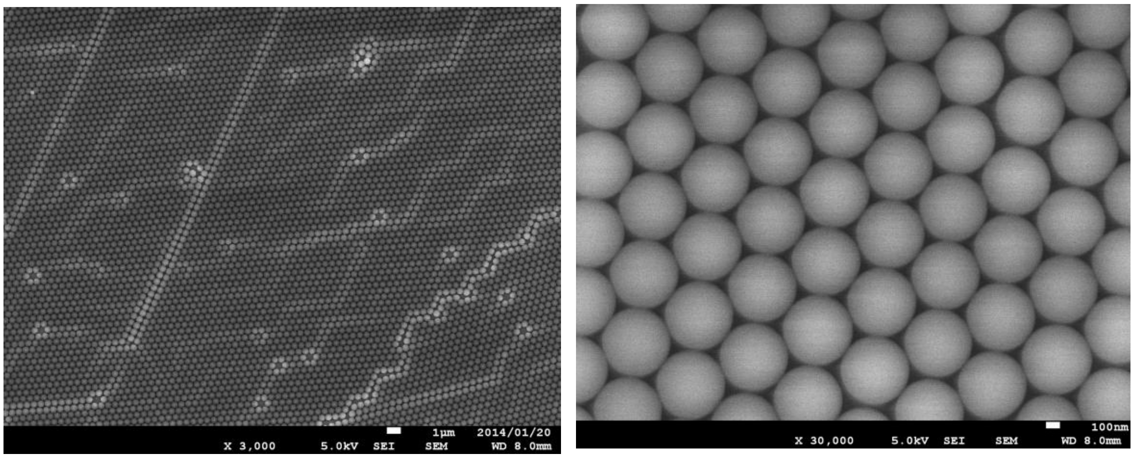

Fig.4.12 Scanning electron microscopy (SEM) images of the coated large areas PS spheres on silicon substrate (a) low-magnification SEM image (b) high-magnification SEM image

Fig. 4.13 shows plane-view SEM images of tailored size of the PS spheres by severally oxygen plasma asing duration, respectively. Fig. 4.13 shows etching duration dependence of diameter of PS sphere estimated from SEM images. Since the position of each bead remained the same after the oxygen plasma etching, the separations between each bead mask increased as the sizes of the beads decreased. Though the etching process, a minor incensement in surface roughness of surface of PS sphere was observed. The heights of the beads were also etched gradually during the oxygen plasma process.

The silicon nanowires prepared with length from 400 nm-1.1 μm using the metal-assisted etching method. The silicon arrays were prepared with in a mixture of deionized water, HF, and H_2O_2. Fig. 4.14 shows the tilted-view (ca. 45°) SEM images of the silicon nanowire arrays. The uniform and vertical Si nanowires were prepared. Etching time can control the length of the nanowires shown in Fig. 4.14 (b). To obtain well-controlled aspect ratio of nanowirs arrays, the etching rate is one of the important parameter. In our case, nanowire arrays can be completed controlled. To simplify the estimation, we define the aspect ratio as the depth of the etched well (length of the wires) divided by the average of the minimum separation between the bead masks and ignore the effect of the etch mask pattern on the etch rate. A graph of silicon substrate etch aspect ratio indicates that the silicon etch rate drops as the aspect ratio increases.

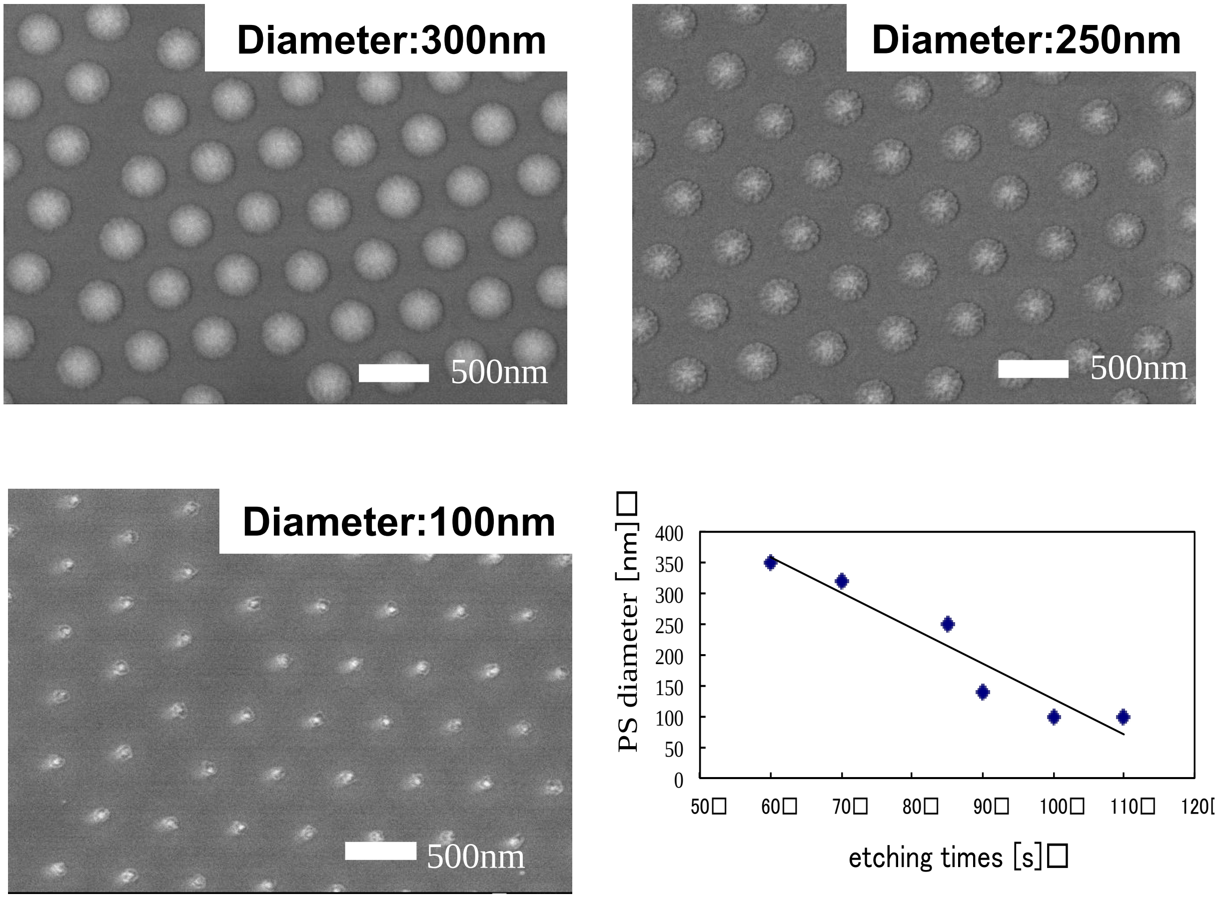

Fig.4.13 plane-view SEM images of tailor the size of the polystyrene spheres with etch time (a) etching 70s (b) etching 85s (c) etching 100s (d) A plot of the diameters of oxygen plasma etched polystyrene beads on silicon substrates versus the plasma etch time.

We have also examined the influence of different Si nanowire length on the optical properties of Si nanowires based wafers. In Fig. 4.15, we show the reflectance spectrum of each length over the wavelength range of 250-850 nm, and the data of a Si wafer is also given for comparison.

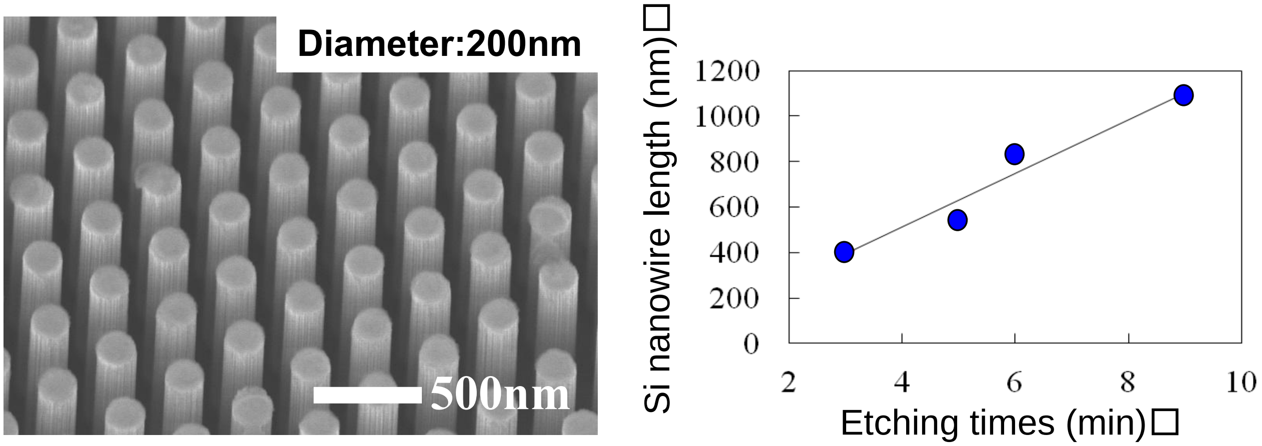

Fig.4.14 (a) tilted-view (ca. 45°) SEM images of the silicon nanowire arrays (b) A plot of the diameters of oxygen plasma etched polystyrene beads on silicon substrates versus the plasma etch time.

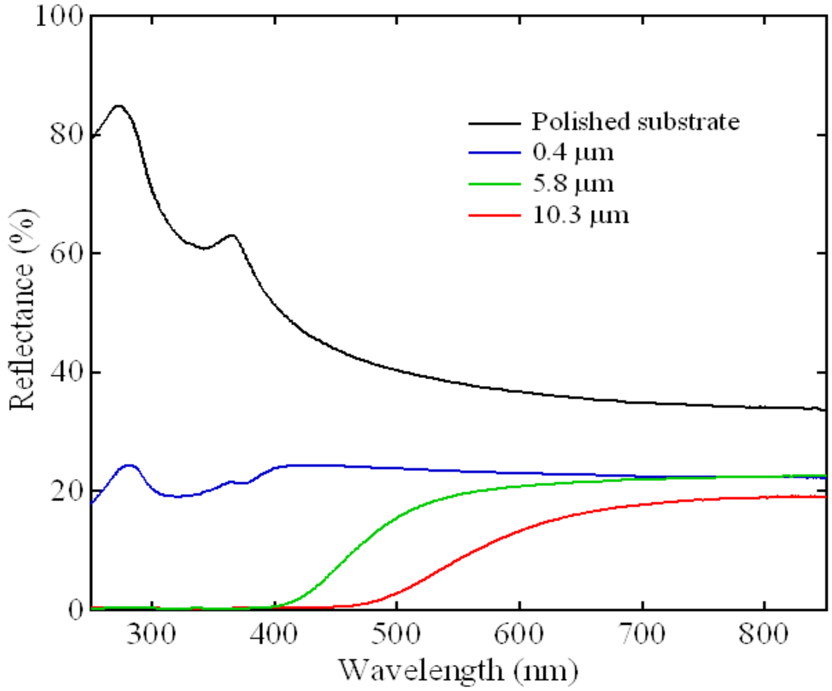

Fig.4.15 Reflection of different silicon nanowire length
(Polished substrate, 0.4 um, 5.8um, 10.3 um)

Clearly, suppressed reflection over entire spectral range is obtained for all series compared to the only wafer, which surely indicates the great improvement of Si nanowires in anti-reflection performance. Also, we can observe that longer Si nanowires have lower reflection than shorter samples. This nanowire length dependent behavior of reflection is mainly attributed to the prolonged optical path length in structure, matching well with the work in the literature [18].

Reference of chapter 4

[1] H. Masuda and K. Fukuda: Science 268 (1995) 1466.

[2] S. Shingubara, O. Okino, Y. Suyama, H. Sakaue, and T. Takahag: Jpn. J. Appl. Phys. 36 (1997) 7791.

[3] O. Jessensky, F. Muller, and U. Gosele: Appl. Phys. Lett. 72 (1998) 10.

[4] W. Lee, R. Ji, U. Go¨sele, and K. Nielsch: Nat. Mater. 5 (2006) 741.

[5] K. Nielsch, F. Mu¨ller, A. P. Li, and U. Go¨sele: Adv. Mater. 12 (2000) 582.

[6] T. Shimizu, M. Nagayanagi, Y. Fujii, O. Yaegashi, G. R. Wu, H. Sakaue, T. Takahagi, O. Sakata, K. Kusaka, and S. Shingubara: Trans. Magn. Soc. Jpn. 4 (2004) 231.

[7] S. Chu, K. Wada, S. Inoue, S. Todoroki, Y. Takahashi, and K. Hono: Chem. Mater. 14 (2002) 4595.

[8] M. Kemell, V. Pore, J. Tupala, M. Ritala, and M. Leskela: Chem. Mater. 19 (2007) 1816.

[9] W. Kim, S. Park, J. Son, and H. Kim: Nanotechnology 19 (2008) 045302.

[10] N. Ji, W. Ruan, C. Wang, Z. Lu, and B. Zhao: Langmuir 25 (2009) 11869.

[11] H. Masuda, M. Yotsuya, and M. Ishida: Jpn. J. Appl. Phys. 37 (1998) L1090.

[12] F. Matsumoto, M. Kamiyama, K. Nishio, and H. Masuda: Jpn. J. Appl. Phys. 44 (2005) L355.

[13] H. Masuda, K. Nishio, and N. Baba: J. Mater. Sci. Lett. 13 (1994) 338.

[14] T. Shimizu, M. Nagayanagi, T. Ishida, O. Sakata, T. Oku, H. Sakaue, T. Takahagi, and S. Shingubara: Electrochem. Solid-State Lett. 9 (2006) J13.

[15] L. A. Nagahara, T. Ohmori, K. Hashimoto, and A. Fujishima: J. Vac. Sci. Technol. A 11 (1993) 763.

[16] Tomohiro Shimizu, Fumihiro Inoue, Chonge Wang, Shintaro Otsuka, Yoshihiro Tada, Makoto Koto and Shoso Shingubara1: Japanese Journal of Applied Physics 52 (2013) 06GF06.

[17] T. Shimizu, T. Xie, J. Nishikawa, S. Shingubara, S. Senz, and U. Go¨sele: Adv. Mater. 19 (2007) 917.

[18] ChenCetal2010Siliconnanowire-array-texturedphotovoltaiccells for photovoltaic application J. Appl. Phys. 108 094318

CHAPER 5

FABRICATION OF CZTS ABSORBER LAYERS USING COST-EFFECTIVE AND LOW-ENVIRONMENTALLY LOADED FORMATION TECHNIQUE

5.1 Background

Electrochemical deposition method has been several reports on the formation of CZTS thin films, such as single step [1], two-step [2], and three step [3, 4] deposition methods. The single step electrochemical deposition process, where all of the required elements are deposited at once in a single electrolyte, has the advantage of simplicity. However, there is a trade-off between the number of processing steps and the ability to control the atomic composition. Therefore, it is difficult to obtain stoichiometric single phase CZTS using the single-step electrochemical deposition method. In contrast, the three-step method, where the required elements are deposited separately using three different electrolytes, enables easier control of the composition ratio, although the number of process steps is increased. The two-step method has intermediate features, such as a relatively small number of processes and good controllability of the atomic composition.

The sulfurization process is very important in the formation of CZTS films, both for supplying sulfur atoms and for improving crystalline. In previous studies on CZTS, the sulfurization process was conducted using H_2S or a solid sulfur source [5, 6]. However, H_2S is a hazardous and highly toxic gas that requires a well-sealed vacuum chamber for safety. With a solid sulfur source, control of the evaporation rate is difficult during the process. For this reason, an additional heater for evaporation of the source or a well-designed chamber with an adequate temperature gradient is required. In contrast, CS_2 is a liquid that can be easily evaporated at room temperature without the need for a complicated vacuum system or heater. Though the CS_2 is one of the toxic materials, high density CS_2 kills living things, but the limit of concentration without hazardous is less than $3.2 mg/m^3$, we can use it in the fume hood. CS_2 is used as a sulfur source for the sulfurization of thermoelectric materials [7, 8]. However, there have been no reports of

CS_2 being used as a sulfurization source for the formation of CZTS. Therefore, we have investigated the formation of CZTS thin film by a combination of a two-step electrochemical deposition of CuSn/CuZn as a precursor and sulfurization of the precursor with CS_2.

5.2 CIGS and CZTS Crystal Structure

CIGS is I-III-VI_2 semiconductor material, CIGS forms chalcopyrite crystal structures when grown in thin film layers [9]. This is the general structure for both CIS and CGS and a bandgap varying continuously from about 1.0 eV to about 1.7 eV. When combined into the alloy, the In and Ga occupy the same sites in the lattice, with their ratio of the total crystal determined by the concentration of the alloy. A unit cell of CIGS is shown in Fig. 5.1 (a). The red spheres represent Cu, the blue spheres either in or Ga depending on the alloy composition and the green spheres show Se. Theoretical predictions show that the (112) surface is the most stable [10], and experimental results support this conclusion [11].

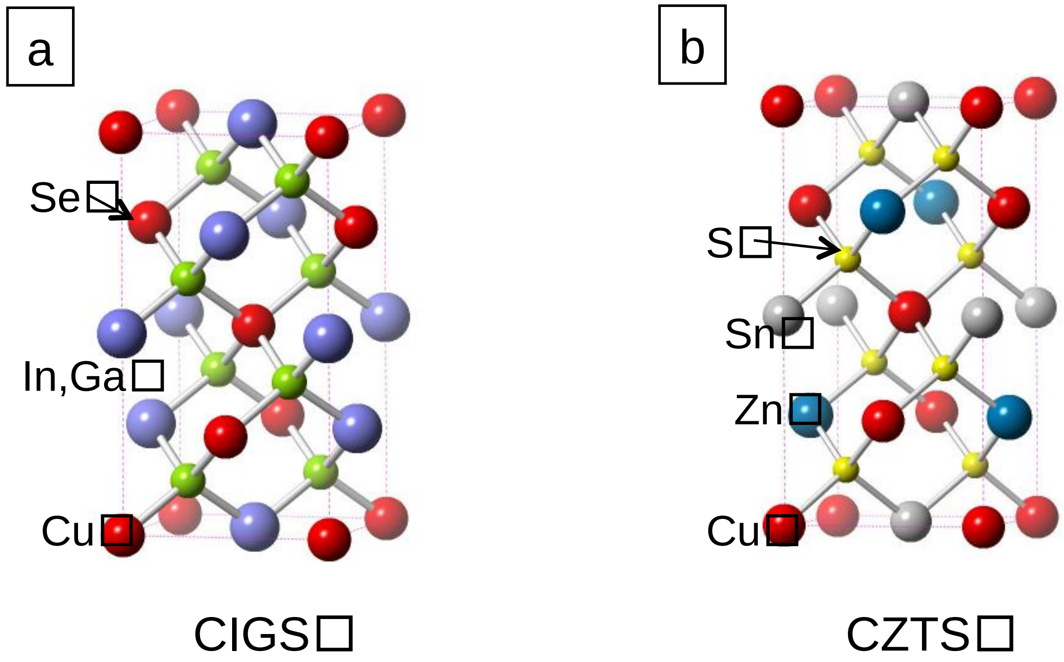

Fig. 5.1(a) Atomic Structure of CIGS (b) Atomic Structure of CZTS

CIGS is a complicated alloy of quaternary structures. It is known that Cu is a mobile atom [12] in the CIGS lattice. This mobility couple with the intentional Cu deficient growth of these films [13,14]. There is experimental evidence for this incorporation, and specifically for the formation of $Cu(In_xGa_{1-x})_3Se_5$ or $CuIn_3Se_5$ for pure CIS within the photovoltaic cell [15-21]. This phase formation is an important component of photovoltaic cell devices.

CZTS is a quaternary I_2-II-IV-VI_4 semiconducting compound. The class of related materials includes other quaternary structure such as copper zinc tin selenium (CZTSe) and the sulfur-selenium alloy CZTSSe. CZTS material is one of the most promising photovoltaic cell materials to replace CIGS absorber layer materials. In spite of CIGS the high efficiency nearly 20%, however, due to containing expensive rare metals of Indium and Gallium, furthermore, CIGS contain toxic element Se, leading to a photovoltaic cell with environmental disadvantage. Therefore, a research about the CZTS photovoltaic cell as a new material device is carried out. CZTS has been confirmed as a promising alternative material for low cost absorber layer in photovoltaic cells because of from CIGS structure, one can obtain CZTS by substituting the trivalent In/Ga with a bivalent Zn and IV-valent Sn, which forms in the structure similar with CIGS. CZTS crystal structure is shown in Fig. 5.1 (b), the red spheres, blue spheres, gray spheres and yellow spheres represent Cu, Zn, Sn and S, respectively. We can know that the composition ratio of CZTS is Cu:Zn:Sn:S=2:1:1:4 from CZTS chemical formulation and crystalline structure. CZTS offers favorable optical and electronic properties similar to CIGS making it well suited for use as a thin film photovoltaic cell absorber layer.

In addition, the crystallization of CZTS is complex. CZTS has three fundamental crystal structures. One is the kesterite structure shown in Fig. 5.2(a), which is derived from the chalcopyrite structure. The other two are the stannite structure (Fig. 5.2(b)) and the primitive mixed CuAu-like structure (Fig. 5.2(c)), both derived from the CuAu-like structure [22].

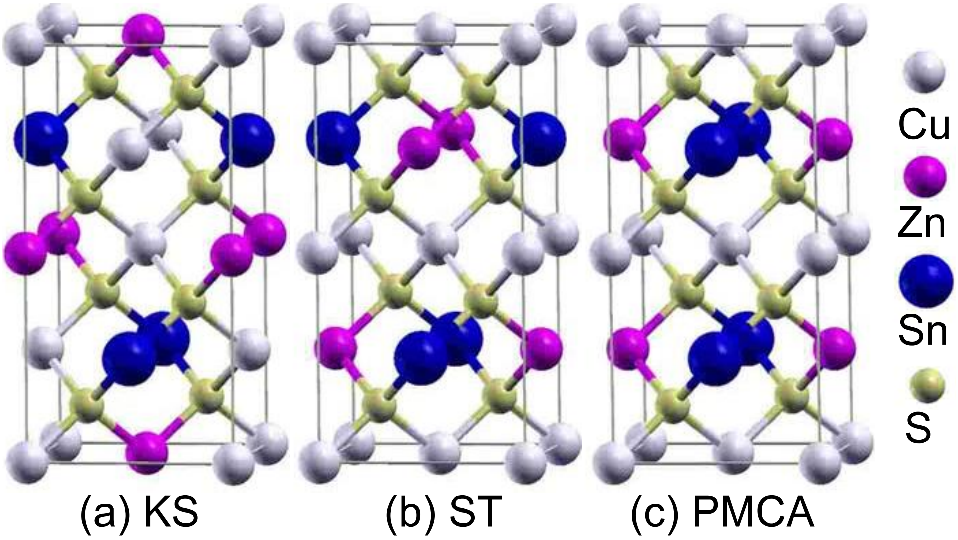

Fig. 5.2 The crystal structure of CZTS in (a) kesterite structure (b) stannite structure (c) primitive mixed CuAu-like structure. [22]

5.3 Electrochemical deposition method

Fig. 5.3 shows a schematic representation of a three-electrode setup used commonly in electrochemical deposition. Two of the electrodes, that is, the working electrode and the counter electrode, are connected to the power source. The substrate is connected as the working electrode, and an inert electrode, often a Pt wire or plate, is used as the counter electrode. The third electrode, that is, the reference electrode, is needed in potentiostatic electrochemical deposition where the potential of the working electrode is controlled in a predetermined manner. The potentiostat measures and controls the potential of the working electrode with respect to the reference electrode and predetermined potentials, and adjusting the current that flows between the working electrode and the counter electrode attains this. The potential of the reference electrode must be known, and furthermore it must stay constant during the deposition. To satisfy the latter requirement, no current is allowed to flow through the reference electrode. Silver-silver chloride electrode (Ag/AgCl) and calomel electrode ($Hg/HgCl_2$) are examples of commonly used reference electrodes.

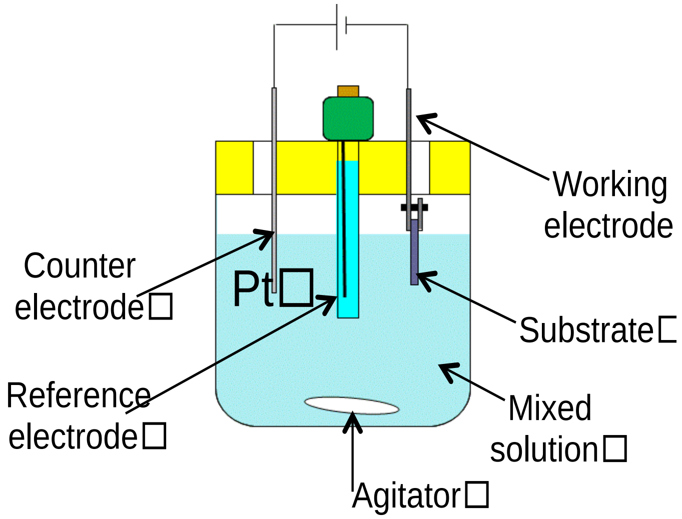

Fig. 5.3 Schematic view of the three-electrode setup used in electrochemical deposition

The mechanism of electrochemical deposition is in the cathode reduction reaction of metal ions, reaction equation as follows:

$$M^{2+} + 2e \rightarrow M^0$$

Deposited on the solid surface, on the other hand, the dissolution of anode in the following reaction:

$$M^0 \rightarrow M^2+ + 2e$$

Metal ions are from the electrolyte.

In this work, we want fabricate CuZn and CuSn two layers thin films using electrochemical deposition method. We can see in Fig. 5.4 (a) and (b) shows the SEM surface and cross-section images of formed CuZn thin film. We can observe the CuZn thin films were uniform and relatively smooth surface. However, using this electrochemical deposition device to fabricated the CuSn thin films on the smooth CuZn thin film, CuSn thin film is not smooth, Fig. 5.5 shows the photo of CuZn/CuSn thin films using electrochemical deposition method, we can know that only the edge of the CuZn thin film formed the CuSn thin films (a part of gray).

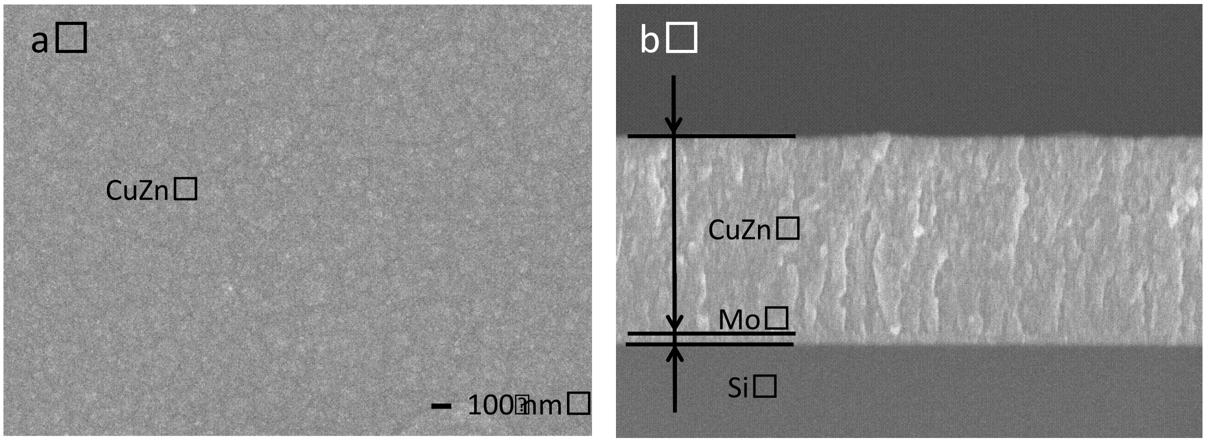

Fig. 5.4 SEM image of CuZn (a) Surface (b) cross-section

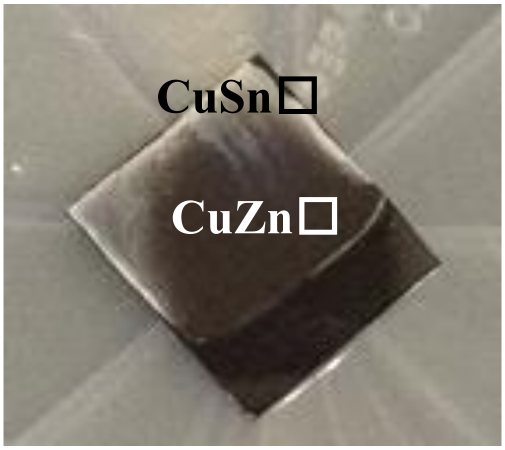

Fig. 5.5 Photo of CuZn/CuSn thin films using electrochemical deposition method

Considering that due to the substrate is a form of hanging, CuSn thin film is not easy to form on CuZn substrate, so we adopt a new electrochemical deposition device shows in Fig. 5.6, the substrate at the bottom of the electrolyte, it is easy to form a uniform CuSn thin films. The uniform CuSn was fabricated by the device of the substrate at the bottom of the electrolyte shows in the Fig. 5.7.

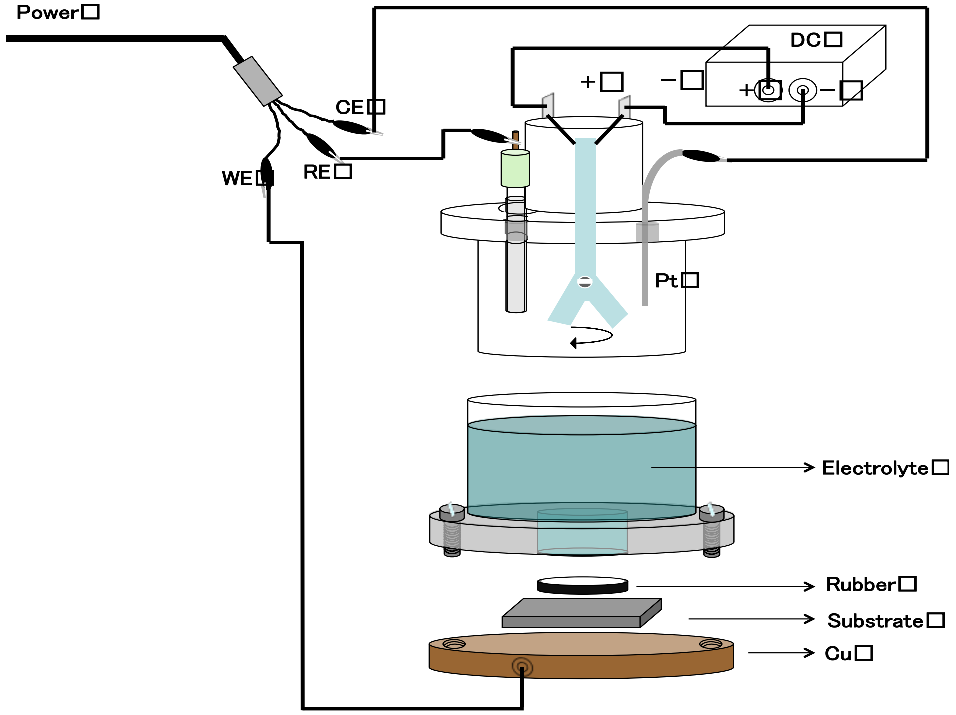

Fig. 5.6 Schematic representation of the three-electrode setup electrochemical deposition device

Fig. 5.7 Photo of CuZn/CuSn thin films using the device of the substrate at the bottom of the electrolyte

5.4 Sulfurization method with CS_2

The fabricated CuZn/CuSn films were sulfurized with CS_2. The schematic of furnace is shown in Fig. 5.8. The precursor was located in furnace center. Argon gas flow from the left, and flows through an empty bottle (to prevent the reverse flow) into CS_2 liquid bottle. CS_2 is a liquid that can be easily evaporated at room temperature, evaporated CS_2 gas and Argon gas flow in the furnace, CS_2 and substrate precursor react to generate CZTS thin films, the excess gas continues to flow until react with bleach, reaction equation as follows:

$$CS_2 + 6NaOH + 8NaClO \rightarrow Na_2CO_3 + 2NaSO_4 + 8NaCl + 3H_2O$$

CS_2 , NaOH and NaClO to react to generated the security Na_2CO_3 , $NaSO_4$, 8NaCl and $3H_2O$. Finally the gas flow through the $KMnO_4$ is security removed.

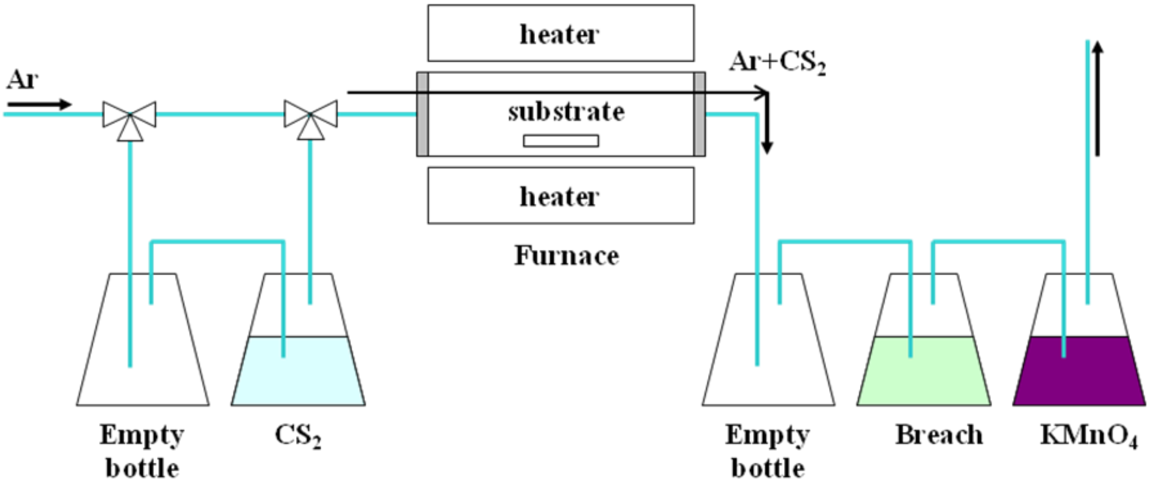

Fig. 5.8 Schematic diagram of sulfurization furnace

5.5 Sample Preparation

Fig. 5.9 shows the main experiment processes for the synthesis of CZTS thin films. First, Mo was deposited by sputtering, Subsequently, the CZTS precursor was prepared by a two-step electrochemical deposition method, which sequentially deposits CuZn and CuSn alloy films on a Mo-coated Si substrate. Then, the deposited films were annealed an 250^{O}C-650 ^{O}C in sulfur atmosphere.

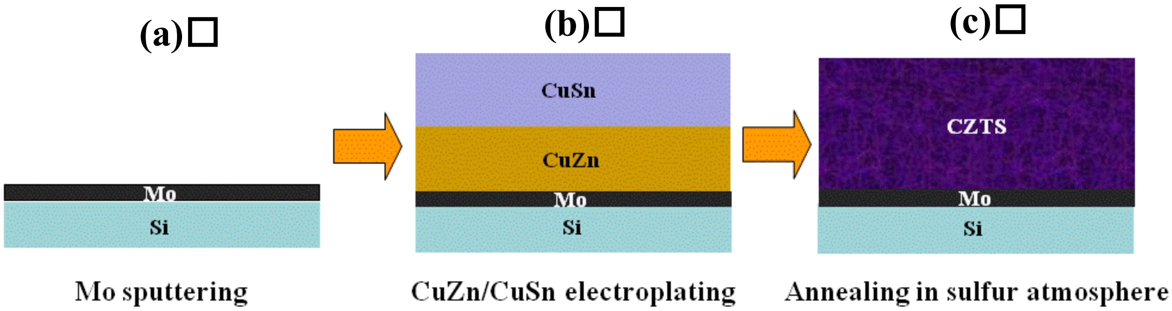

Fig.5.9 Schematics of the sample preparation (a) Mo film is sputtered on Si substrate (b) CuZn and CuSn thin films are deposited by two-step electrochemical deposition (c) Sulfurization of CuZn/CuSn thin films was carried out by annealing in CS_2+Ar gas atmosphere.

CuZn was prepared from an aqueous electrolytic bath containing 0.02 M copper (II) sulfate pentahydrate ($CuSO_4{\cdot}5H_2O$), 0.2 M zinc sulfate heptahydrate ($ZnSO_4{\cdot}7H_2O$), 1 M tri-sodium citrate ($C_6H_5Na_3O_7$: Na_3-citrate) as a complexing agent, and NaOH for pH control. CuSn deposition was performed with an aqueous electrolyte containing 0.02 M copper (II) sulfate pentahydrate ($CuSO_4{\cdot}5H_2O$), 0.1 M $SnCl_2$, and 0.5 M tri-sodium citrate ($C_6H_5Na_3O_7$: Na_3-citrate) as a complexing agent. Electrochemical deposition was performed using a potentiostat (HZ-5000, Hokuto Denko) in DC mode with a three-electrode configuration. The electrochemical cell contained a saturated Ag/AgCl electrode as a standard reference electrode, a platinum (Pt) electrode as an inert counter electrode, and a Mo-coated substrate with an area of 1.5×1 cm^2 as the working electrode. Fig. 5.10 shows the dependence of the CuZn and CuSn alloy composition ratios on the deposition potential. The composition ratio of the alloys was dependent on the deposition potential, with Cu:Zn and Cu:Sn ratios of 1:1 obtained at around -1.2 and -0.7 V, respectively. The CZTS precursor films were prepared by the sequential deposition of CuZn and CuSn layers onto the Mo-coated electrode. The atomic ratio in the precursor film was adjusted to Cu:Zn:Sn = 2:1:1, which is the stoichiometry of CZTS without sulfur, by control of the deposition potential and thickness of each layer.

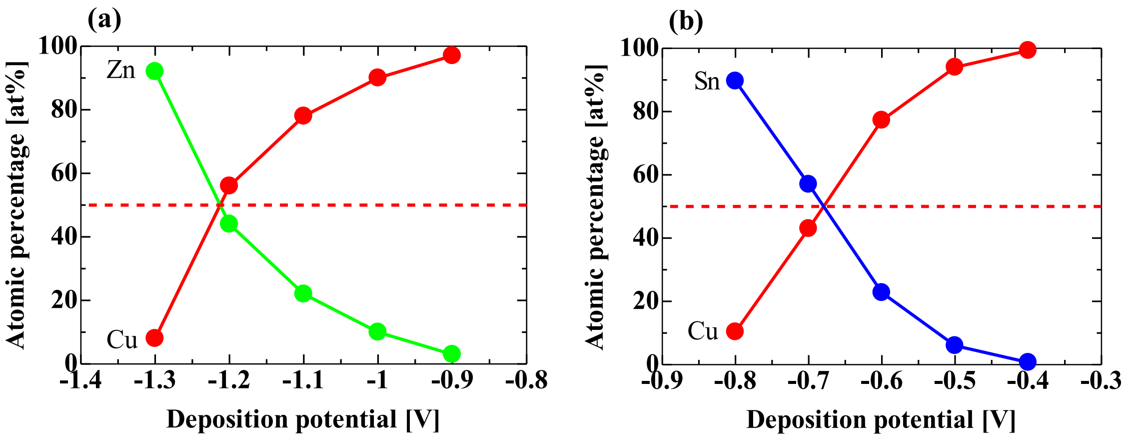

Fig. 5.10 Variation in the atomic percentage of CuZn and CuSn thin films as a function of deposition potential.

Subsequently, sulfurization of the precursor was performed using a CS_2 source at 250–650 ^{O}C. The thermal annealing profiles are depicted in the Fig. 5.11. The precursor substrate is pre-annealed at 350 ^{O}C for 10 minute and sulfide at 250, 450 and 650 ^{O}C for 50 minutes, respectively.

Binary and ternary compounds are formed at low temperature through reactions and fabrication of CZTS occurs at higher temperature during sulfurization [23].

Reaction process is as following:

(1) $Cu + S \rightarrow CuS$

(2) $Cu_2 + S \rightarrow Cu_2S$

(3) $Sn + S_2 \rightarrow SnS_2$

(4) Zn + S ➔ ZnS

(5) $Cu_2S + SnS_2$ ➔ Cu_2SnS_3

(6) $Cu_2SnS_3 + ZnS$ ➔ Cu_2ZnSnS_4

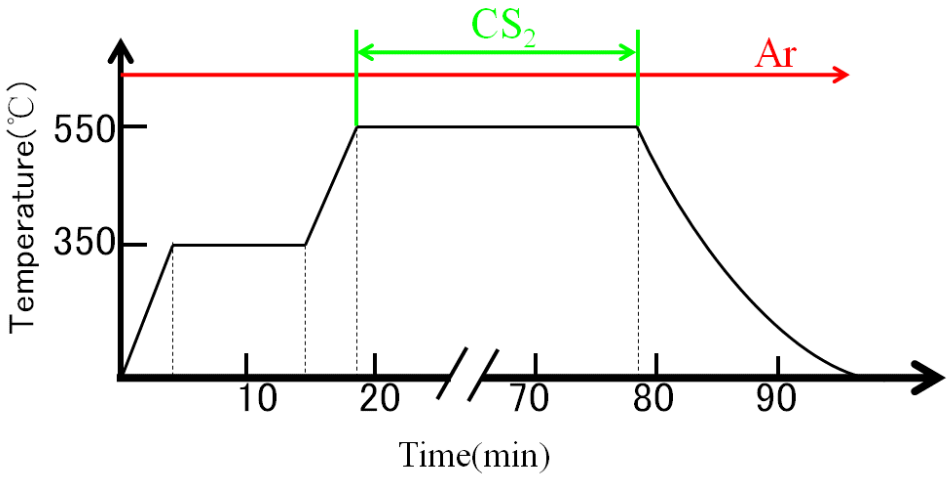

Fig. 5.11 The thermal annealing profiles of samples.

5.6 Result and discussion

The crystal structures of the samples were evaluated using X-ray diffraction (XRD, PHILIPS, X-ray with CuKα radiation, λ= 1.5406 Å,). The room temperature Raman scattering spectra were recorded by a JOBIN YVON T64000 with 487 nm lasers. The surface morphological, Elemental mapping images and compositional study of the formed films were performed by using field emission scanning electron microscopy (FE-SEM, Model: JSM-3000F, JEOL, Japan) attached with an energy-dispersive X-ray spectrometer (EDS) to measure the sample composition. Cross-sectional transmission electron microscopy (TEM; JSM-2100F, JEOL) was performed to observe the CdS/CZTS/Mo/substrate structure. Energy-dispersive X-ray (EDX) spectroscopy was conducted using the EDX system installed in the TEM. The chemical binding energies of the precursor and the annealed CZTS films were measured using X-ray photoelectron spectroscopy (XPS; ESCA-3400, SHIMADZU) at room temperature. Optical properties of the samples were analyzed by UV-VIS spectrophotometer. Photoluminescence (PL) was performed at room temperature and low temperature using an excitation diode laser with a wavelength of 325 nm.

5.6.1 Chemical composition characterization

The dependence of the chemical composition of the CZTS precursor thin films sulfurized at various temperatures were demonstrated by the EDS measurement and shown in Table 1.

Table 1: The elemental composition of the precursor and CZTS thin films sulfurized at different temperatures.

Temperature	Atomic %				Ratio		
	Cu	Zn	Sn	S	Cu/Zn+Sn	Zn/Sn	S/Metal
precursor	48.06	27.45	24.49	—	0.93	1.1	—
250 ^{O}C	47.32	25.59	24.48	2.61	0.95	1.0	0.03
450 ^{O}C	22.35	14.48	11.57	51.60	0.86	1.2	1.1
650 ^{O}C	17.48	6.85	5.20	70.47	1.45	1.3	2.4

After sulfurization, both Cu/(Zn + Sn) and Zn/Sn vary with the different temperature. At 250 ^{O}C Zn/Sn ratio minor changes from 1.1 to 1.0 and only about 2.61 % of sulfur element was observed, indicating that the sulfur element has not begun to react with the elemental of Cu, Zn, Sn in precursor, only a small amount of sulfur element attached on the surface of the precursor. With the temperature increased to 450 ^{O}C, the elemental composition of CZTS thin films was nearly stoichiometry with Cu/(Zn + Sn) ratio of 0.86 and Zn/Sn ratio of 1.2, this result was consistent with slightly Cu-poor and Zn-rich elemental composition can lead to good optoelectronic properties according to previous research by Katagiri et al [24]. Moreover, the S/metal ratio of the CZTS thin film is greater than 1, indicating that sulfur has been sufficiently incorporated into the films. Continue to increase the temperature to 650 ^{O}C, we noticed that Cu/(Zn + Sn) ratio increases to 1.45 while Zn/Sn decreases slightly and S/metal ratio increased to 2.4, indicating that Zn and Sn elementals of CZTS thin films a lot of loss during at the high temperature of 650 ^{O}C. These changes can be attributed to the re-evaporation of Zn and Sn from thin film surface during the sulfurization period. It is concluded from above results that the atomic ratio of Cu:Zn:Sn:S in CZTS thin films can be effectively controlled by adjusting the sulfurization conditions.

5.6.2 X-ray diffraction measurements

The structural properties of the as-deposited and sulfurized precursor films were evaluated from XRD measurements.

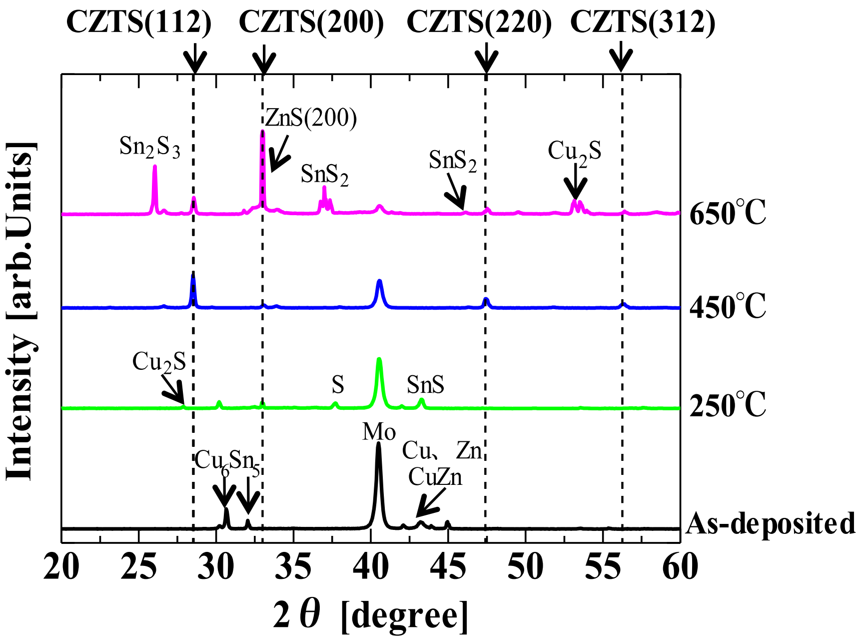

Fig. 5.12 XRD patterns for CuSn/CuZn precursor thin films and CZTS thin films annealed at various temperatures from 250 to 650 °C.

Fig. 5.12 shows typical XRD patterns for the CZTS precursor thin films sulfurized at various temperatures. The peaks detected for the as-deposited CuSn/CuZn precursor are associated with Cu (111), Zn (101), CuZn (110), Cu6Sn5 (311), and Mo (110), which come from the deposited CuZn and CuSn alloy layers and the substrate. The precursor films sulfurized in CS_2 at 250 °C have XRD peaks at 26-27°, 33° and 43-44°, which suggests the presence of Cu_2S (002), ZnS (200) and SnS (002). The formation of these compounds at a low sulfurization temperature below 250 °C has been reported by other groups using H2S or solid sulfur as sources [25]. The samples annealed above 450 °C showed several peaks belonging to CZTS (112), (200), (220) and (312), which indicates the formation of polycrystalline CZTS films. Moreover, at 450 °C, all of the peaks were identified as kesterite CZTS and no additional impurity peaks were detected, except for Mo peaks from the substrate. Several alloys, such as SnS_2 (0, 1, 14), Sn_2S_3 (111), ZnS (200), and Cu_2S (200), were detected for the film annealed at 650 °C. These XRD results indicate that the use of CS_2 as a sulfur source provides almost the same results as those for conventional sulfurization using H_2S or S sources [26].

5.6.3 Raman spectra

To identify the phase purity of CZTS in the sulfurized films, Raman spectroscopy was performed owing to difficulty of peak separation of CZTS from impurity phase of ZnS, Cu_2SnS_3 (CTS) by XRD measurements. Fig. 5.13 shows the Raman scattering spectra of precursor and films annealed at different temperatures from 250 ^{O}C to 650 ^{O}C with 487 nm excitation wavelengths. The observed spectra indicated that CZTS and impurity compound, in particular MoS_2, were formed at 650^{O}C. At 450 ^{O}C, the Raman peaks at 287cm^{-1}, 338cm^{-1} and the peak at 367.8cm^{-1} confirm only CZTS. It is noticeable that the peaks at 274cm^{-1}, 351cm^{-1} and 693cm^{-1} attributed to the Zinc hybrid ZnS do not appear, suggesting the absence of this compound [27, 28]. The precursor and the substrate of 250^{O}C have not appeared Raman peak between the 200cm^{-1} and 600cm^{-1}. These results are well agreed with XRD measurement, and these result strongly suggested that almost single-phase CZTS films were obtained by sulfurization at 450 ^{O}C using CS_2 source.

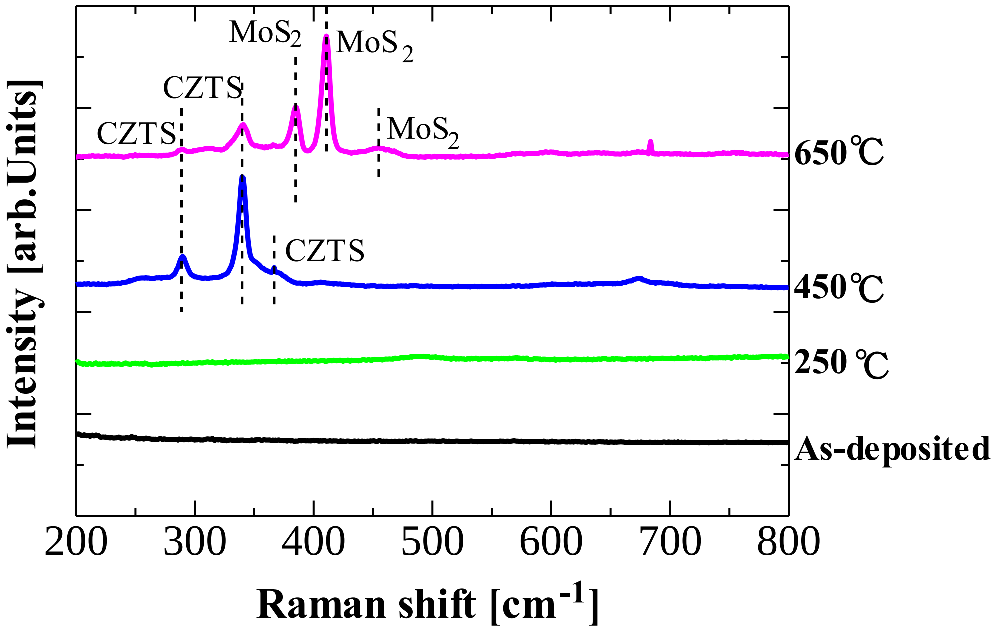

Fig. 5.13 Raman scattering spectra of precursor and films annealed at different temperatures from 250 ^{O}C to 650 ^{O}C.

5.6.4 Cross-sectional TEM characterization and electron diffraction pattern

Fig. 5.14(a) shows a cross-sectional TEM image of the CdS/CZTS/Mo p-n structure. A CdS buffer layer was formed by the chemical bath deposition (CBD) method on the CZTS film after sulfurization. Although the surface of the CZTS film was rough, the CdS film was continuous and conformed to the CZTS surface.

The thickness of the CdS and CZTS layers were 70 nm and ca. 1 um, respectively. Large grains in the CZTS film (ca. 100 nm diameters) tend to grow on the upper side of the CZTS film, while small grains are observed at the bottom of the film, near the Mo back contact. The elemental composition ratio was determined from the EDX measurements and the results are shown in Table 2. In the large top grain (locations 1 and 2), almost stoichiometric CZTS was observed, and Zn rich compositions were observed in the small bottom grain (location 5). Fig. 5.14(b) shows selected area electron diffraction (SAED) pattern obtained at the white circle area indicated in Fig. 5.14(a). The SAED pattern is well indexed to kesterite-type CZTS projected along the [110] direction. Assuming kesterite-type CZTS, the lattice spacing was estimated from the diffraction spots using the following equation:

$$r_{hkl}d_{hkl}=\lambda L, \tag{5.1}$$

where d_{hkl} is the (*hkl*) lattice spacing, r_{hkl} is the distance between diffraction spot and direct spot, λ is the wavelength of the incident electron, and L is the camera length of the microscope. The estimated lattice spacing d [110] is close to the theoretical value 3.84 Å, this result confirm that the CZTS have a kesterrite phase [29].

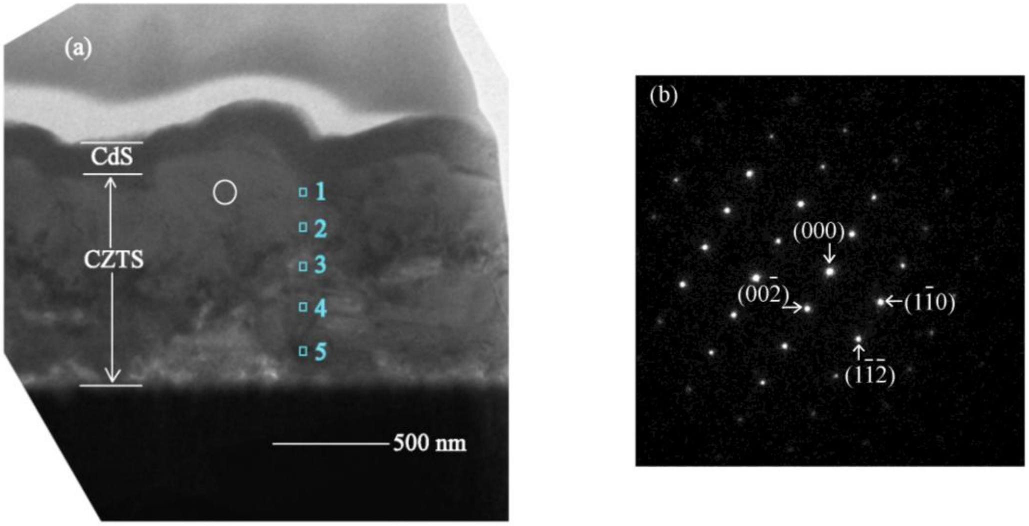

Fig. 5.14 Bright-field TEM image of CZTS thin film; (a) TEM image of the CdS/CZTS/Mo/substrate structure, and (b) Corresponding SAED pattern obtained at the white circle area indicated in Fig. 4.11(a).

The crystallographic TEM observations were consistent with the XRD measurements, which suggest that the CZTS film has an almost single-phase kesterite structure without any secondary phases. The Zn rich phase at the bottom of the film would be formed by evaporation of Sn during sulfurization. This could be avoided by preparing a precursor that contained excess Sn over stoichiometry.

5.6.5 Morphological characterization

Fig.5.15 displays the SEM surface morphologies for CuZn/CuSn precursor and CZTS thin films prepared at different sulfurization temperatures. It can be seen that before sulfurization, the film is the superposition of CuZn and CuSn alloy thin films in Fig. 5.15 (a). The film minor changes At 250 ^{O}C were observed shown in Fig. 5.15 (b). This is metallic phases. With the increase of the temperature to 450 ^{O}C, the CZTS begin to form and the grain size from tens of nm up to a few hundred nm shows in Fig.5.15 (c). The grain size will be the limiting factor for the carrier lifetime and does not satisfy the requirement for the fabrication of high performance device [30].

Moreover, the film surface is rougher and more porous although the grain size is increased, which is detrimental to the improvement of conversion efficiency. With the increase of the temperature to 650 ^{O}C shows in Fig.5.15 (d), the film surface becomes relatively more uniform, and the grain size becomes larger than 450 ^{O}C, indicating that the grain growth is enhanced at higher temperature. However, not only the binary sulfides were formed, but also leads to a damage of the Mo back contact film at 650 ^{O}C.

Table 2: Composition of CZTS thin films determined from EDX spectra.

Location of CZTS in Fig.4.11(a)	Cu	Zn	Sn	S	Cu/(Zn+Sn)	Zn/Sn	S/CZT
1	29.96	15.08	12.74	42.19	1.08	1.18	0.73
2	30.66	14.69	13.25	41.19	1.10	1.11	0.70
3	29.67	14.67	14.42	41.24	1.02	1.02	0.70
4	29.99	13.46	11.62	44.49	1.20	1.16	0.81
5	24.55	19.92	8.25	46.14	0.87	2.41	0.88

Cross-sectional SEM images of the sulfurized CZTS thin films are shown in Fig. 5.16. It can be seen that before sulfurization, the film is the superposition of CuZn and CuSn alloy thin films (Fig. 5.16a). At 250 ^{O}C the film did not have any change, including the thickness and the size of the particles (Fig. 5.16b). With the increase of the temperature to 450 ^{O}C (Fig. 5.16c), CZTS begin to form and the film is thicker than the precursor from about 0.4 um to 1.6 um and the grain size from tens of nm up to a few hundred nm. With the increase of the temperature to 650 ^{O}C (Fig. 5.16d), not only the binary sulfides was formed, but also leads to an damage of the Mo back contact film. Therefore, in terms of thickness and the particle size, 450 ^{O}C is the most suitable for sulfurization of CZTS thin films.

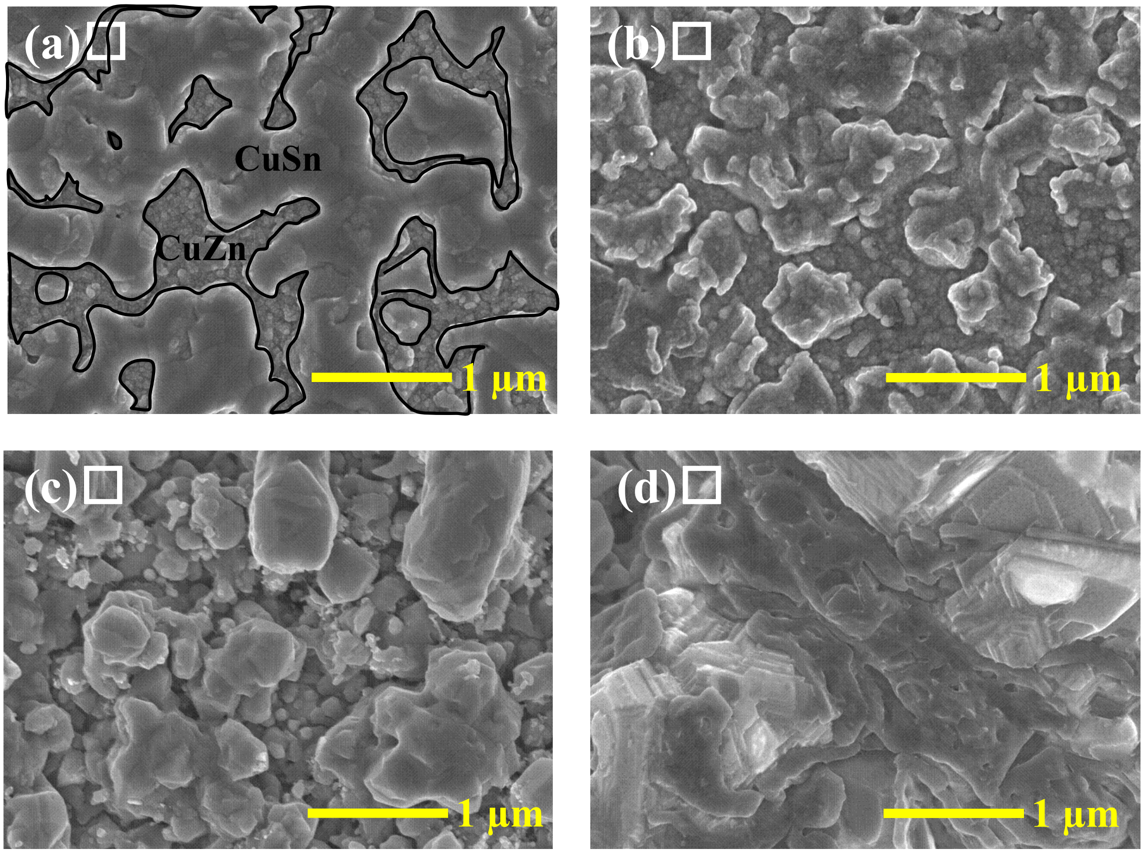

Fig. 5.15 SEM micrographs of CuSn/CuZn precursor and CZTS films annealed at various sulfurization temperatures (a) As-deposited, (b) 250 ^{O}C, (c) 450 ^{O}C, (d) 650 ^{O}C.

5.6.6 Carbon element composition characterization

Carbon element compositional analysis of the CZTS thin films was performed using

XPS. Typical survey spectra of the as-deposited precursor and that for a CZTS thin film sulfurized at 450 °C are shown in Fig. 5.17(a). After sulfurization, the spectrum for CZTS indicates the presence of Mo, Cu, Zn, Sn and S. Additionally, before sulfurizaiton a small amount of adventitious carbon C1s was incorporated from the carbon in the starting material. Indicated by the C1s peak shows in the Fig.5.17 (b), the adventitious carbon of binding energy scale is made with respect to 284.5 eV of C1s.

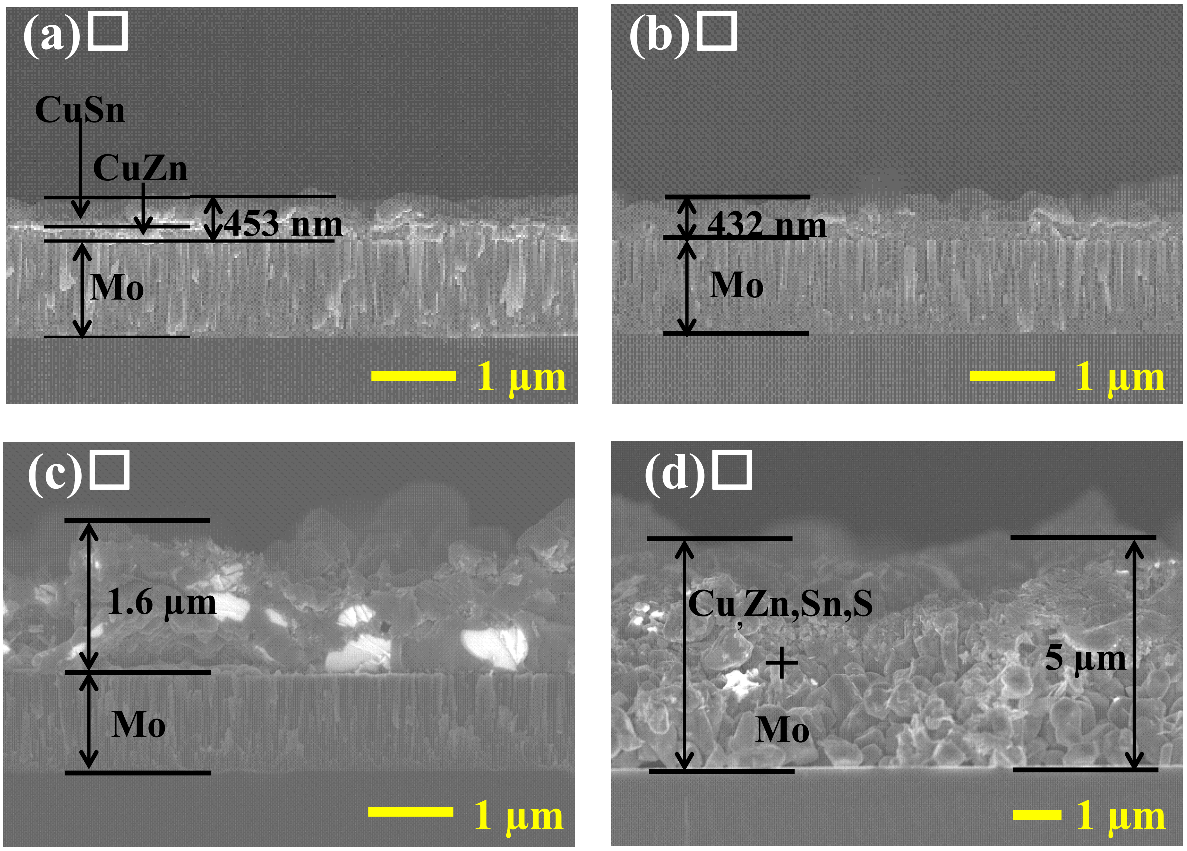

Fig. 5.16 Cross-section SEM image of CuSn/CuZn precursor and CZTS films annealed at various sulfurization temperatures (a) As-deposited, (b) 250 ^{O}C, (c) 450 ^{O}C, (d) 650 ^{O}C.

The intensity and position of the C1s peak did not change substantially after sulfurization, which suggests that the carbon in the CZTS film did not come from the CS_2 source during sulfurization. If there were any undecomposed CS_2 in the film, the C 1s peak would shift to the positive side. Therefore, from the XPS studies, it is confirmed the formation of CZTS phase after sulfurization treatment and the carbon did not come from the CS_2 source during sulfurization.

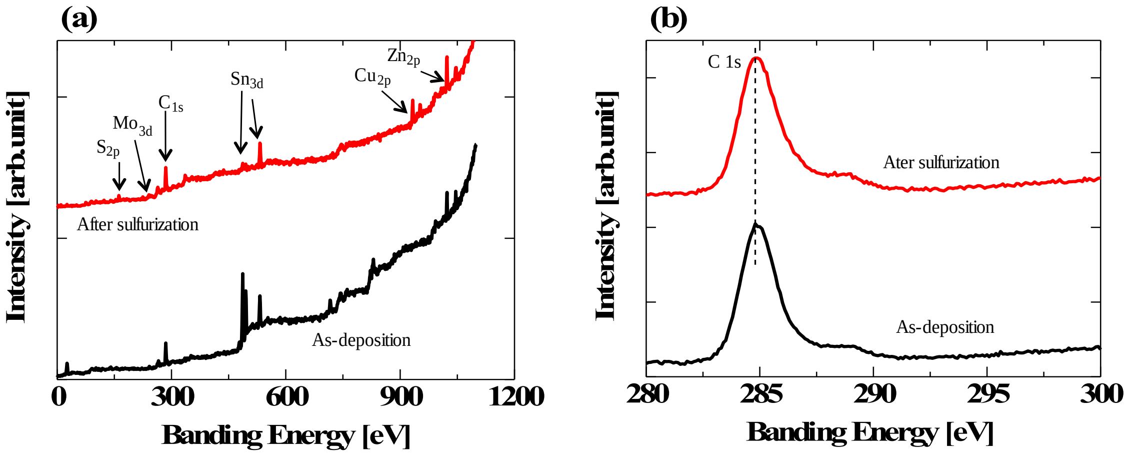

Fig. 5.17 XPS spectra for CZTS thin films (a) XPS survey spectrum of CZTS sample (b) Curve of the C 1s peak.

5.6.7 Optical characterization (UV-Vis spectrometer)

In Fig. 5.18 the room temperature optical reflection spectra of thin films with respect to different sulfurization temperature were compared. At the As-deposition stage, the film reflects the light in a broad wavelength range; the overall reflection is relatively high especially in the visible region. This can be attributed, incorporation of metallic phase in the film.

By sulfurization at a low temperature of 250°C for 50 minutes, the film reflects the light were reduced significantly, but in the visible region is still relatively high reflection. Visibly, alloy materials still exist in thin films. When sulfurization at high temperature of 450°C for 50 minutes, the film reflects the light were reduced significantly in a broad wavelength range from 300 nm to 850 nm. This can be attributed, the CuZn, CuSn and reaction of alloy phase vanished, at this stage has already formed the CZTS thin films. Thus, the reflectivity reduced. Sulfurization temperature continue rise to 650 OC, reflectivity has increased, this is because of the Mo was sulfide, caused the reflectivity to rise. In fact, we can pass the measure reflectivity to determine the bandgap of CZTS materials; the bandgap of CZTS is about in 800-900 nm wavelengths, due to the limited of measure equipment, and now still cannot determine the bandgap of CZTS via the UV-Vis reflection spectroscopy. But the next PL measurement method will determine the bandgap of CZTS materials.

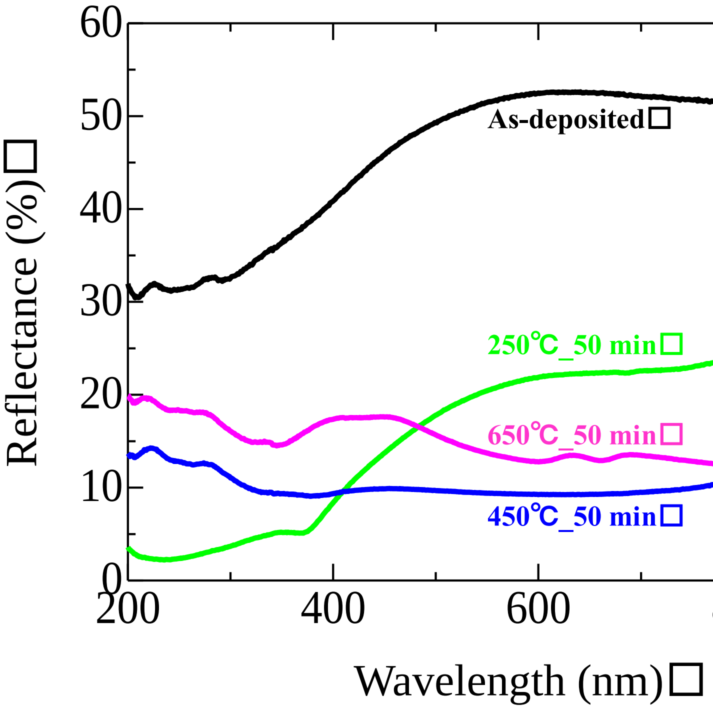

Fig. 5.18 Optical reflection spectra of thin films with respect to different sulfurization temperature

5.6.8 Optical characterization (Photoluminescence (PL))

In order to study the recombination mechanism, the photo- luminescence of CZTS thin film was measured. Fig. 5.19 shows the photoluminescence spectra of CZTS film recorded at room temperature. The sample show broad PL band centered at about 1.38 eV, 1.51eV and 1.65 eV at room temperature, one band is smaller than the corresponding optical band gaps. This observation points to the defect related type recombination in CZTS thin films. The absence of transitions from band to band in PL spectra may be attributed to the fact that defect type recombination is the dominant recombination channel in this material due to the large number of possible intrinsic defects in CZTS material [31]. The band of 1.65 may be is the MoS_2, Because of Mo easy to sulfide at high temperature, and the band of MoS_2 is about 1.8 eV.

Single-phase CZTS thin film was successfully prepared using a non-vacuum process. CuSn/CuZn precursor films were prepared by a two-step electrodeposition method on a Mo back contact film and annealing in a CS_2 atmosphere performed sulfurization of the precursor. The optimum sulfurization condition for the precursor was 450 °C for 50 min. XRD, Raman, XPS and TEM measurements indicated that the annealed CZTS thin films have a kesterite structure, although a few grains of a Zn-rich phase were observed at the bottom of the CZTS film. The combination of electrodeposition and CS_2 sulfurization can realize low cost CZTS formation and could be used for the production of large area CZTS films, such as those required for low cost photovoltaic cells.

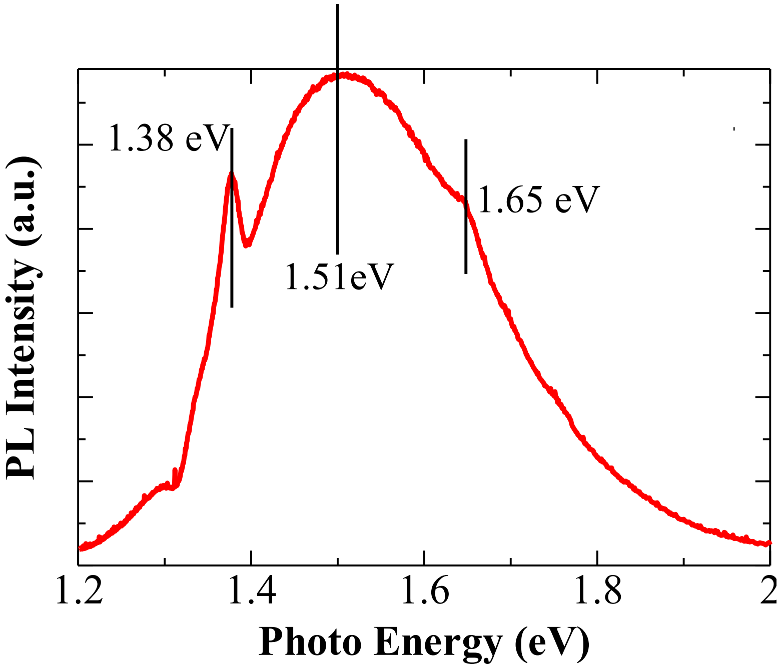

Fig. 5.19 PL spectra of annealed samples at room temperature

References of chapter 5

[1] M Jeon, T Shimizu and S Shigubara, Mater Lett. 65 (2011) 2364-2367.

[2] M.Ganchev, L.Kaupmees, J.Iliyna, J.Raudoja, O. Volobujeva, H. Dikov, M.Altosaar, E.Mellikov and T.Varema, Energy Procedia. 2 (2010) 65–70.

[3] R. Schurr, A. Holzing, S. Jost, R. Hock, T. Voss, J. Schulze, A. Kirbs, A. Ennaoui, M. Lux-Steiner, A. Weber, I Kotschau, HW. Schock, Thin Solid Films. 517 (2009) 2465–2468.

[4] Yixin Lin, Shigeru Ikeda, Wilman Septina, Yoshihito Kawasaki, Takashi Harada and Michio Matsumura, Photovoltaic Energ Mater Photovoltaic Cells.120 (2014) 218–225.

[5] JJ. Scragg, PJ. Dale, LM. Peter, Thin Solid Films. 517 (2009) 2481–2484.

[6] K. Moriya, K. Tanaka, H. Uchiki, Jpn. J. Appl. Phys. 47 (2008) 602-604.

[7] M. Ohta, HB. Yuan, S. Hirai, Y. Uemura, K. Shimakage, J Alloys Compounds. 374 (2004) 112-115.

[8] N. Sato, G. Shinohara, A. Kirishima, O. Tochiyama, J Alloys Compounds. 451 (2008) 669-672.

[9] C. Persson and A. Zunger, Phys. Rev. Lett. 91, 266401 (2003).

[10] K. Ito, T. Nakazawa: Jpn J Appl Phys. 27 (1988) 2094-7.

[11] S. Sadewasser, Th. Glatzer, M. Rusu, A. Jäger-Waldau, and M. Ch. Lux-Steiner, Appl. Phys. Lett. 80, 2979 (2002).

[12] C. Persson and A. Zunger, Appl. Phys. Lett. 87, 211904 (2005).

[13] I. L. Repins, M. A. Contreras, B. Egaas, C. DeHart, J. Scharf, C. L. Perkins, B. To, and R. Noufi, Prog. Photovolt. Res. Appl. 16, 235 (2008).

[14] K. Ramanathan, M. A. Contreras, C. L. Perkins, S. Asher, F. S. Hasoon, J. Keane, D. Young, M. Romero, W. Metzger, R. Noufi, J. Ward, and A. Duda, Prog. Photovolt: Res. Appl. 11, 225-230 (2003).

[15] M. A. Contreras, H. Wiesner, R. Matson, J. Tuttle, K. Ramanathan, and R. Noufi, Mat. Res. Soc. Proc. 426, 243 (1996).

[16] S. Han, A. M. Hermann, F. S. Hasoon, H. A. Al-Thani, and D. H. Levi, Appl. Phys. Lett. 85, 576 (2004).

[17] S. Han, F. S. Hasoon, H. A. Al-Thani, A. M. Hermann, and D. H. Levi, Appl. Phys. Lett. 86, 021903 (2005).

[18] R. Herberholz, U. Rau, H. W. Schock, T. Haalboom, T. Gödecke, F. Ernst, C. Beilharz, K. W. Benz, and D. Cahen, Eur. Phys. J. AP 6, 131-139 (1999).

[19] D. Liao and A. Rockett, Appl. Phys. Lett. 82, 2829 (2003).

[20] M. J. Romero, K. M. Jones, J. AbuShama, Y. Yan, M. M. Al-Jassim, and R. Noufi, Appl. Phys. Lett. 83, 4731 (2003).

[21] D. Schmid, M. Ruckh, F. Grunwald, and H. W. Schock, J. Appl. Phys. 73, 2902 (1993).

[22] S.Y. Chen, X. G. Gong, A. Walsh, and H.W. Su, Applied Physics Letters, 94 (2009) 041903.

[23] R.Schurr, A. Holzing, S. Jost, R. Hock, T. Vos, J. Schulze, Thin Solid films, 517 (2009) 2465.

[24] H. Katagiri, K. Jimbo, W. S. Maw, K. Oishi, M Yamazaki, H. Araki, A.Takeuchi, Thin Solid Films. 517 (2009) 2455–2460.

[25] R.B.V. Chalapathy, G. S. Jung and B. T. Ahn, Photovoltaic Energ Mater Photovoltaic Cells.95 (2011) 3216–3221.

[26] N. Kamoun, H. Bouzouita, B. Rezig, Thin Solid Films. 515, (2007) 5949-52.

[27] PA. Fernandes, PMP. Salome, AF. da Cunha, Thin Solid Films. 517 (2009) 2519-2523.

[28] PA. Fernandes, PMP. Salome, AF. da Cunha, J Alloys Compounds. 509 (2011) 7600-7606.

[29] YF. Liu, MY. Ge, Y. Yue, Y. Sun, YZ. Wu, X. Chen and N. Dai, Phys. Status Solidi. 5 (2011) 113–115.

[30] T.K. Todorov, J. Tang, S. Bag, O. Gunawan, T. Gokmen, Y. Zhu, D.B. Mitzi, Adv. Energy Mater. 3 (2013) 34.

[31]A. Nagoya, R. Asahi, R. Wahl, G. Kresse, Phys. Rev. B 81 (2010) 113202.

CHAPTER 6

FABRICATION OF CZTS NANOSTRUCTURE ARRAYS USING BOTTOM-UP APPROACHES

6.1 Fabrication of CZTS nanowire arrays

6.1.1 Background

In recent years, fabrications of CZTS absorber layer using variety methods have been reported. Electroplating method has several advantages, such as simple, low cost, non-vacuum, large area deposition and room temperature growth. In 2011 year, our research group reported that fabrication of CZTS thin films and nanowires by single-step electrodepositing method, The CZTS thin film and nanowire with kesterite structure have been formed shows in Fig.6.1, however, it is difficult to control the composition ratio of CZTS. In this chapter, we synthesize CZTS nanowires by two-step electroplating method with AAO template and the sulfurization temperature was change. The structural, morphological and compositional characteristics of the CZTS nanowires and thin films were investigated and discussed.

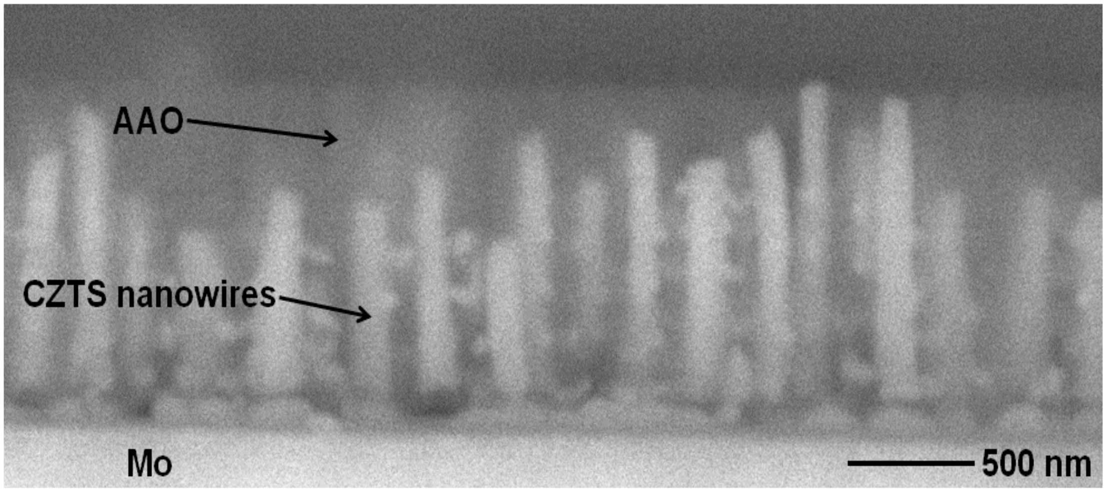

Fig. 6.1 SEM image of CZTS nanowires using single-step electro-depositon method

6.1.2 Sample preparation

Using the CZTS thin films fabrication conditions to prepared the CZTS nanowires. Fig.6.2 shows the experiment processes of CZTS nanonwires using two-step electrodepositon into AAO template. First, Mo and Al films were deposited on Si substrates by sputtering, and the Al films were anodized in 0.3 M oxalic acid at 40V potential. After anodization, AAO pore slightly etched to remove the alumina layer at the pore bottom. Subsequently, CuZn and CuSn were alternately electroplated into AAO nanoholes using the same electroplating condition of deposit thin films. After electroplating AAO mask was completely removed from Mo surface by selective etching. The deposited nanowires were sulfurized of at 600℃ for 10 min. We used the electrodepositon conditions, which had been optimized for preparation of CZTS nanowires in our previous study.

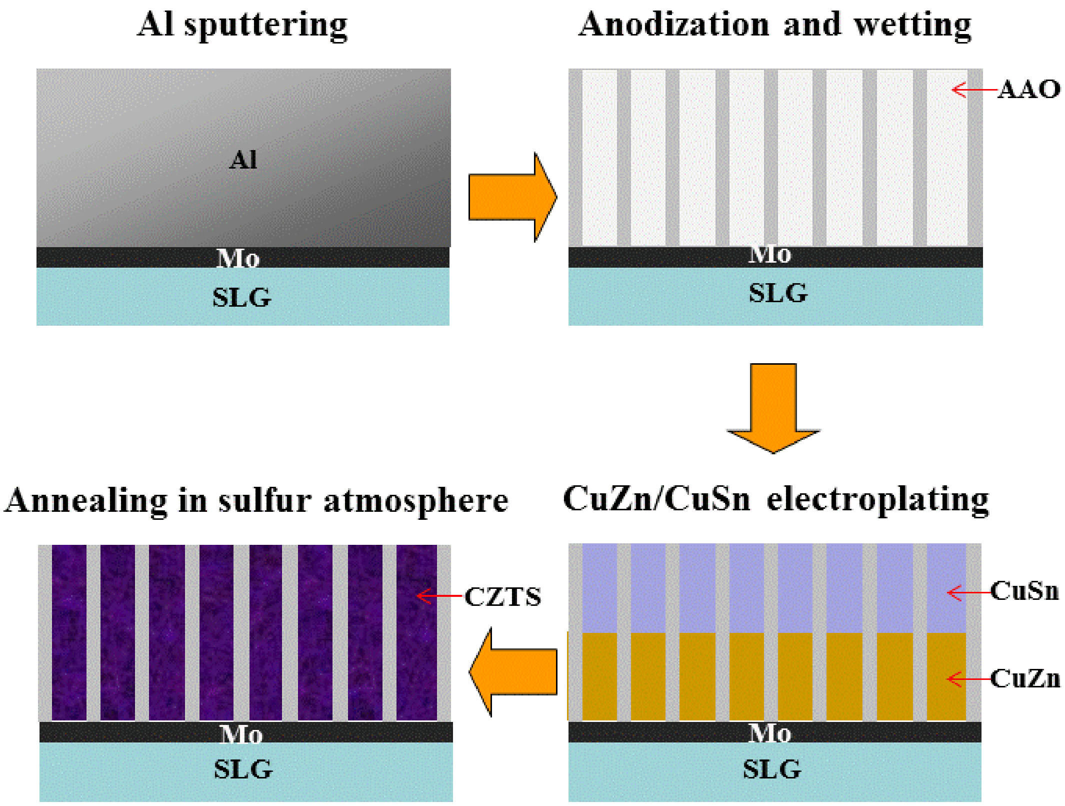

Fig. 6.2 Schematics of the sample preparation

6.1.3 Results

Fig. 6.3 shows XRD patterns of sulfurized CZTS thin films deposited with different annealing temperature. It is seen that all the XRD patterns consist of (100), (112) and (103) diffraction peaks corresponding to different crystallographic planes of CZTS, suggesting that the films are polycrystalline with kesterite crystal structure. From the XRD results, some metal sulfide and other secondary phases, such as CuxS, SnSx, CuxSny, and CuxSnySz were also detected. These secondary phases are often observed in CZTS thin films during the formation process, particularly for the copper-rich chalcopyrite samples [1-4]. From these results, we realized that annealing conditions affect the surface morphologies of prepared CZTS thin film.

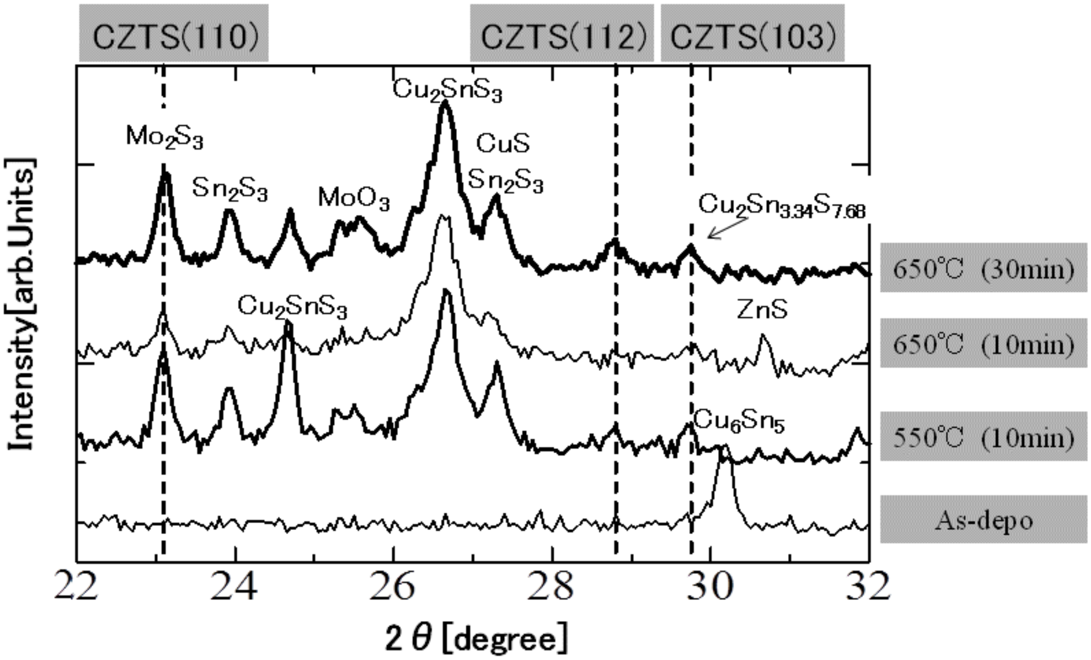

Fig. 6.3: XRD patterns of as-deposited CZTS precursor thin film and CZTS thin films annealed at varies annealing temperatures from 550℃ to 650 ℃

The SEM images of the CZTS nanowires are shown in Fig. 6.4. From Fig. 6.4(a), it can be seen that the vertical CuZn/CuSn nanowires were obtained by two-step electroplating method with AAO template, and the CZTS nanowires' diameter and average length were

70nm and 500 nm. The geometry of the CZTS nanowires, such as diameter and density, can be controlled by the geometry of AAO nanoholes. Fig. 6.4(b) shows the CZTS nanowire arrays after sulfurization at 60 ^{O}C for 10 min in CS$_2$+Ar atmosphere with AAO nanoholes. It can be observed nanowires were still vertical on the Mo-coated Si substrate. We found that the formed nanowires were vertical to the substrate. This can provide the potential application and research for one-dimension photovoltaic cells.

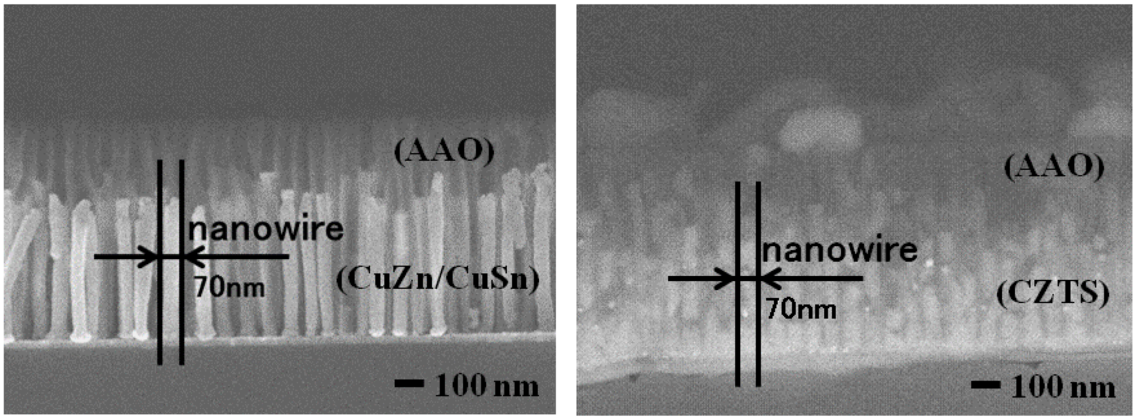

(a) (b)

Fig.6.4 SEM image of electroplated CuZn/CuSn nanowires for as-depositied and after sulfurization: (a) Cross-section SEM image of as-deposited CuZn/CuSn nanowires. (b) after sulfurization at 600℃ for 10 min in CS$_2$+Ar atmosphere with AAO nanoholes.

Vertical CZTS nanowires were fabricated on Mo-coated Si substrates by two-step electroplating method, employing nanoporous anodic aluminum oxide as a template. About the chemical compositions of the CuZn and CuSn with different deposition potential, when the CuZn deposition potential was -1.3V and the CuSn was -0.9V, nearly stoichiometric composition was obtained. The element compositions of CuZn/CuSn nanowires about 2:1:1 was obtained. From the morphology studies, we can conclude that the obtained nanowires are vertical to the substrate. X-ray diffraction patterns indicate that the annealed CZTS thin films have a kesterite structure including secondary metal and metal sulfide phases. We have found that the quality of CZTS nanowires strongly depends on the annealing conditions.

6.2 Fabrication of CZTS nanocylinders

6.2.1 Background

As absorbing layer of photovoltaic cells, the use of one-dimensional structures has attracted a lot of attentions due to its property of high absorbance for visible light. In this part, we tried to prepare vertical CZTS nanocylinder arrays by RF sputtering on substrates using Si nanowire arrays fabricated with a combination of self-assembled polystyrene sphere and metal-assisted etching method as template.

Sputtering method is one of the physical vapor deposition (PVD) techniques for preparation of a film. In the basic sputtering process, the source material, named target, is bombarded by energetic positive ions (inert gas such as Ar or N_2) generated in glow discharge plasma situated in the front of the target. Fig. 6.5 shows illustrates schematically of the RF reactive sputter apparatus. The bombardment process causes the removal, i.e., “sputtering”, of target atoms, which may then condense in a thin film on a desired substrate. The positively charged gas ions from the plasma are attracted and accelerated towards the target by the electric field obtained as a result of applying a negative potential on the target with respect to the substrate electrode. Thus the source electrode for the target is known as cathode, and the substrate electrode anode.

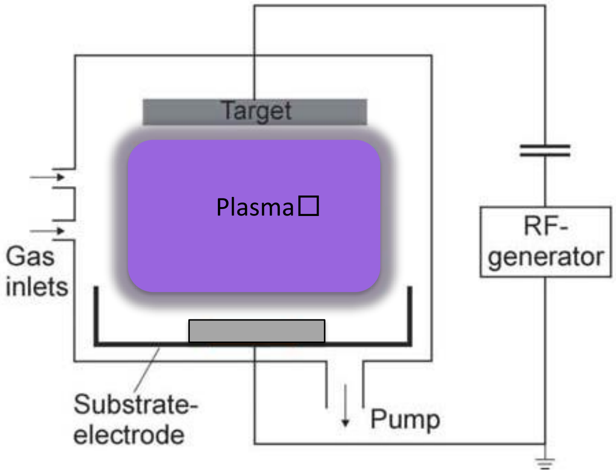

Fig. 6.5 Schematic representation of the RF reactive sputter system

6.2.2 Sputtering of Mo and CZTS

Fabricated Si nanowire arrays were used as a template for the sputtering of Mo back electrode and CZTS thin films. Fig. 6.6 shows sample preparation procedure for CZTS/Mo have cylinder array.

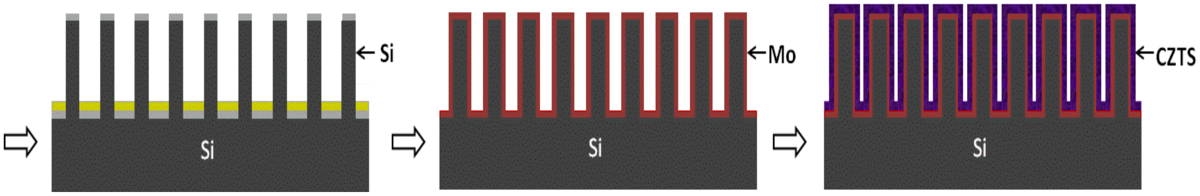

Fig. 6.6 The schematics of the sample preparation using Si nanowire arrays fabricated CZTS nanocylinder

6.2.3 Results

Fig.6.7 shows the SEM image of samples after sputtering of Mo back electrode. The vertically grown Mo coated nanowire arrays with diameter of 300nm and length of 790nm were successfully prepared. We can also see from this image at the bottom of the cross-section image of the nanowires. Black contrast at the bottom of nanowire is part of Si nanowire striped 50 nm Mo layer array.

Subsequently, We prepared of CZTS nanocylinder by RF sputter on coated Mo nanostructure. Fig.6.8 shows the SEM image of samples after sputtering of CZTS on Mo back electrode. The vertically grown CZTS nanocylinder with diameter of 400nm and length of 857nm were successfully prepared. Mo thin film is continuous and the thickness is about 50 nm. We can conclude by calculation of the CZTS thickness of about 50 nm. However, we obtained the thin film of CZTS nanocylinder is not uniform. The sidewall of the CZTS nanocylinder is about 50 nm, the thickness of the bottom is about 70 nm and the top of CZTS nanocylinder is about 300 nm. Let`s worry about most is where there have the discontinuous at the bottom.

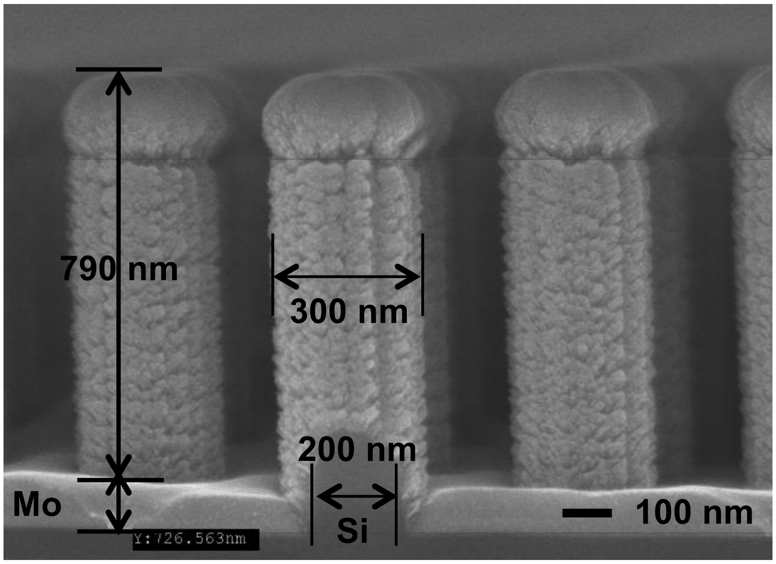

Fig. 6.7 SEM image of samples after sputtering of
Mo back electrode

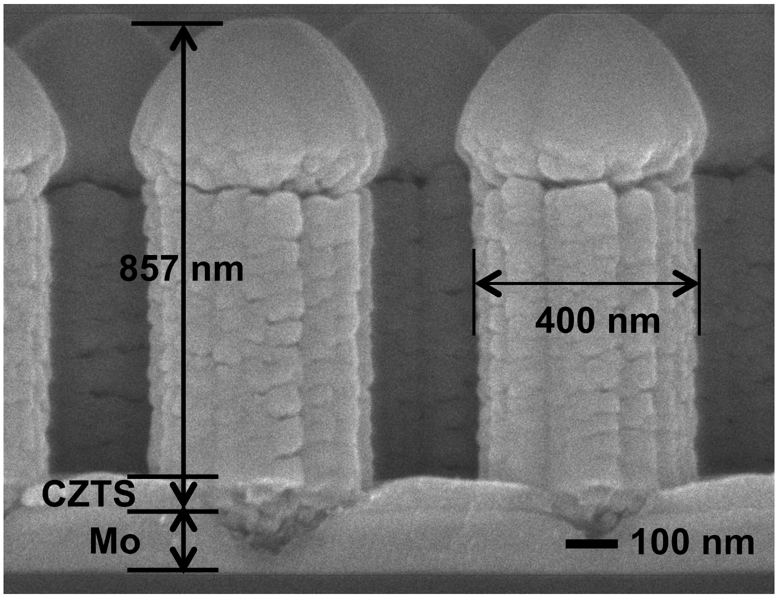

Fig. 6.8 SEM image of samples after sputtering of
CZTS absorber layer

The optical reflectance spectra for three kind of length of CZTS nanocylinders are shown in Fig. 6.9. The CZTS nanocylinder show a reduction in reflectance of about 15%

over the measured whole spectrum range spectrum ranging from 200 to 900 nm. We note that no additional antireflective layer was employed in either the nanowire or planar samples. Visually, the nanocylinder structure has a matte finish and are significantly darker in appearance compared to the planar films.

In addition, the length of nanocylinders also is affected for reflectivity. The 1200 nm length nanocylinder structures indicated a reduction of reflectance about 2% from 400 nm length nanocylinder structures in visible range.

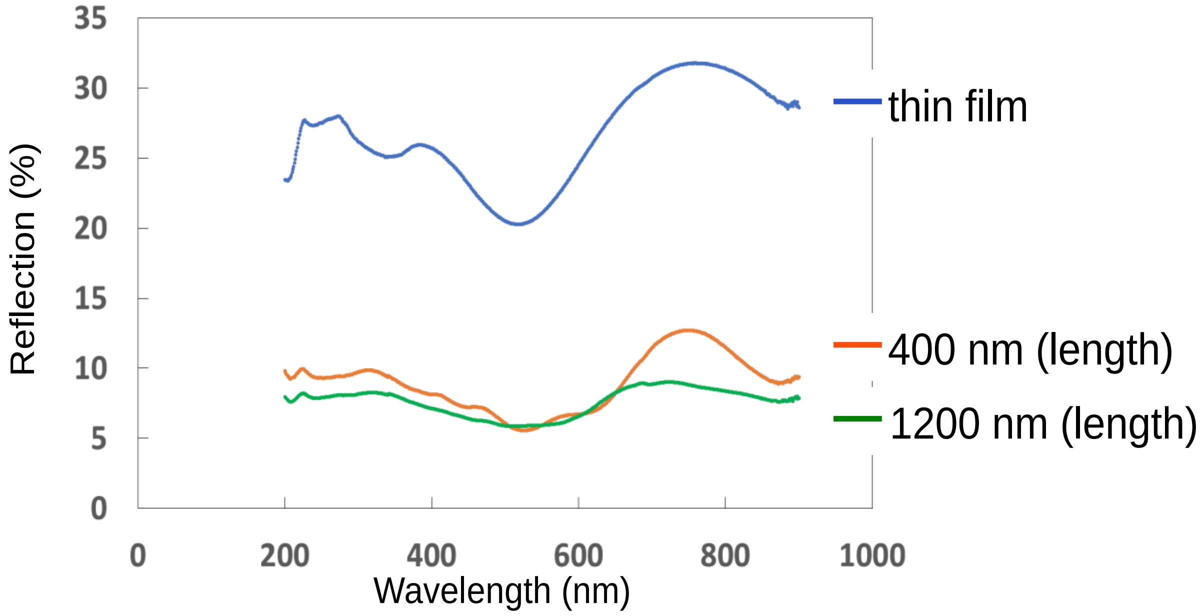

Fig.6.9 Reflectance of different CZTS nanocylinder length

Especially, reflectance around 750 nm shows drastic reduction depending the wire length. This reduction would come from enhancement of light absorption due to light trapping effect of nanowire arrays. Generally, the light trapping effect caused by nanowire arrays strongly depends on size of inter-wire distance and diameter of the wire. In fact, compound with Fig. 4.15 and Fig. 6.9, the wire length of absorbed light was changed because diameter and sistance of wire was totally different.

Thus, this results imply light wavelength tuning of absorbance world be realized using a control of size of wire array. Finally, we concluded that CZTS nanocylinder structure to reduce the reflectance and improve the optical have effective. CZTS nanocylinder will be apply on the photovoltaic cell is worth waiting for.

References of chapter 6

[1] I. Repins, M. Contreras, B. Egaas, C. DeHart, J. Scharf, C. Perkins, B. To, R. Noufi ,Progress in Photovoltaics: Res Appl 16(3) (2008) 235-239.

[2] K. Ito, T. Nakazawa, Jpn J Appl Phys 27 (1988) 2094-7.

[3] T. Tanaka, T. Nagatomo, D. Kawasaki, M. Nishio, Q. Guo, A. Wakahara, A. Yoshida, H. J Phys Chem Solids 66 (2005) 1978-81.

[4] B.M. Kayes, H.A. Atwater and N.S. Lewis, Journal of Applied Physics 97 (2005) 114302-1 −114302-11.

CHAPTER 7

SUMMARY AND FUTURE WORK

Although various techniques have been performed to produce Si and CZTS absorber layers, the efficiencies of photovoltaic cells based on Si and CZTS have been limited to around 25% and 11.1 % to date, respectively, CZTS conversional is still very low due to the relatively low quality of the CZTS absorber layers and insufficient knowledge about the fundamental properties of the absorber material.

In my work, we used the nanostructure to increasing the optical characterization of crystalline Si and CZTS absorber layer. I have focused on using the VLS method to obtain vertical Si nanowires and using the metal-assistant etching to obtain the low cost CZTS nanocylinders. My experiments found that the CZTS nanocylinder structure can reduce in reflectance about 15% over the full spectrum ranging from 200 to 900 nm. This results show that the nanostructure to improve the conversion efficiency with big possibility.

In order to achieve the goal, three methods were used to fabrication of vertical nanowire structure. These results are summarized as follows:

- We have demonstrated control of growth direction, crystal orientation of Si nanowires epitaxially grown on Si (111) and (110) substrate using an AAO template and catalytic VLS growth with silane gas. The Si nanowires were grown parallel to Si [111] and [110] on the Si (111) and (110) substrate, respectively. The crystal orientation of the nanowire can be selected by choosing Si substrate cut in desired orientation.

- Single-phase CZTS thin film was successfully prepared using a non-vacuum process. CuSn/CuZn precursor films were prepared by a two-step electrodeposition method on a Mo back contact film and annealing in a CS_2 atmosphere performed sulfurization of the precursor. The optimum sulfurization condition for the precursor was 450 °C for 50 min. XRD, Raman, XPS and TEM measurements indicated that the annealed CZTS thin films have a kesterite structure, although a few grains of a Zn-rich phase were observed at the bottom of the CZTS film. The combination of electrodeposition and CS_2 sulfurization can realize low cost CZTS formation and could be used for the production of large area CZTS films, such as those required for low cost photovoltaic cells.

- Vertical CZTS nanowires were fabricated on Mo-coated Si substrates by two-step electroplating method, employing nanoporous anodic aluminum oxide as a template. About the chemical compositions of the CuZn and CuSn with different deposition potential, when the CuZn deposition potential was -1.3V and the CuSn was -0.9V, nearly stoichiometric composition was obtained. The element compositions of CuZn/CuSn nanowires about 2:1:1 was obtained. From the morphology studies, we can conclude that the obtained nanowires are vertical to the substrate. X-ray diffraction patterns indicate that the annealed CZTS thin films have a kesterite structure including secondary metal and metal sulfide phases. We have found that the quality of CZTS nanowires strongly depends on the annealing conditions.

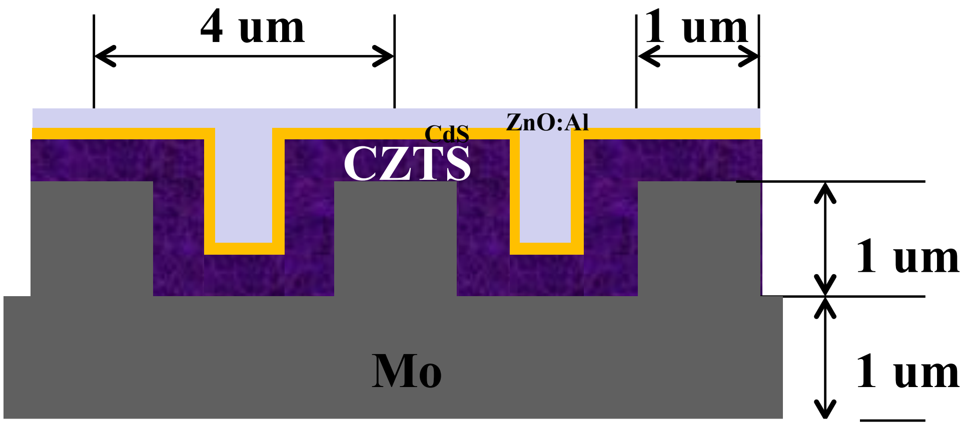

Fig. 7.1 Typical nanostructure photovoltaic cell

- The morphology of the nanostructure on the Si substrate after metal assisted etching and optical reflectance of each morphology were fabricated. We found that CZTS nanowire diameter and length were depended on the PS diameter and metal assisting etching tims. In addition, optical reflection was depended on de nanocylinder length, and

CZTS nanocylinder shows low reflectance value. This result would help and accelerate the development of low cost photovoltaic cells.

- Industrial production and commercialization of CZTS photovoltaic cells continues to be an important goal of research into CZTS material systems. Fig. 7.1 shows the typical photovoltaic cell structure. There are a wide variety of growth methods for photovoltaic cells structure. It is important to note that in the multilayered structure each layer deposited with a different process. The purpose of the growth is to obtain the highest quality material possible at the lowest cost of production. An additional consideration for practical manufacturing is to have a growth process that is easily scaled to large areas to further reduce costs during photovoltaic cell production.

Appendices

Acronyms

TW	Terawatt
CIGS	$CuInGaSe_2$
CZTS	Cu_2SnZnS_4
PV	Photovoltaic
1D	One-dimensional
VLS	Vapor-liquid-solid
AAO	Anodized aluminum oxide
XRD	X-ray Diffraction
TEM	Transmission Electron Microscopy
BF	Bright Field
DF	Dark Field
SEM	Scanning Electron Microscopy
XPS	X-ray Photoelectron Spectroscopy
EDX	Energy-Dispersive X-ray
PL	Photoluminescence
FWHM	Full Width at Half Maximum
SADP	Selected Area Diffraction Pattern
ESCA	Electron Spectroscopy for Chemical Analysis
AAO	Anodic aluminum oxide)
LP-CVD	Low-pressure chemical vapor deposition

PS	Polystyrene
CBD	Chemical bath deposition

List of publications

(Accepted Journal Papers with Review)

1. ChongE. Wang, Shukichi Tanaka, Tomohiro Shimizu and Shoso Shingubara. "Fabrication of vertical Cu_2ZnSnS_4 nanowire arrays by two-step electroplating method into anodic aluminum oxide template", Journal of Material Science and Nanotechnology, (2014) accepted for publication

2. ChongE Wang, S.Tanaka, K.Saitoh, T. Shimizu, and S. Shingubara, "Fabrication of an ordered anodic aluminum oxide pore arrays with an interpore distance smaller than the nano-indentation pitch formed by ion beam etching", Journal of Material Science and Nanotechnology (2014) accepted for publication

3. T. Shimizu, F. Inoue, ChongE Wang, S. Otsuka, Y. Tada, M. Koto, S. Shingubara, "Control of Crystal Orientation and Diameter of Silicon Nanowire Using Anodic Aluminum Oxide Template", Jpn. J. Appl. Phys, **52**, 06GF06-04 (2013)

(Submitted Journal Papers under Review)

1. ChongE Wang, T. Shimizu, A.Kondo, S. Tanaka, Y. Tominari and S. Shingubara. "Fabrication of Cu_2ZnSnS_4 thin films using two-step electrochemical depositions and non-vacuum CS_2 sulfurization", Thin Solid Films.

(Related Papers with Review)

1. T. SHIMIZU, Q. WANG, ChongE WANG, F. INOUE, M. KOTO, M. JEON, S. SHINGUBARA, “Control of Crystal Orientaion of Epitaxial Si nanowires on Si Substrate Using AAO template”, Materials Research Society, 1350, EE03-02 (2011)

2. T.YAMAGUCHI, T. SHIMIZU, F. INOUE, ChongE Wang, S. Otsuka, Y.tada, Y.Morosawa, K. Tanaka, M.Inada and S. SHINGUBARA, “Control of the Morphology of Si Nanostructure Using Single-step Metal Assisted Etching Method”, ECS Transactions, 50,109-115 (2013)

3. T.YAMAGUCHI, T. SHIMIZU, ChongE Wang, M. INADA, S. SHINGUBARA, A. KUZNETSOV, J. VANACKEN, V. MOSCHALKOV, “Evaluation of crystal structure of porous Si nanowires prepared by metal assisted etching”, Materials Research Society, 1439. AA03-02 (2012)

(Conference Presentations and Proceedings)

1. ChongE Wang, Yasuharu Ishida, Shukichi Tanaka, Ken-ichi Saitoh, Tomohiro Shimizu, and Shoso Shingubara
"Fabrication of an ordered anodic aluminum oxide pore arrays with an interpore distance smaller than the nano-indentation pitch formed by ion beam etching"
IMFEDK 2012.5 Osaka

2. ChongE Wang, Yoshinori.Tanaka, Toshifumi Terui, Shukichi Tanaka, Tomohiro Shimizu and Shoso Shingubara
"Fabrication of Cu_2ZnSnS_4 nanowire arrays using electroplating with nanohole template"
JSAP 2012.9, Ehime

3. ChongE Wang, Yoshinori.Tanaka, Toshifumi Terui, Shukichi Tanaka2, Tomohiro Shimizu and Shoso Shingubara
"Fabrication of vertical Cu_2ZnSnS_4 nanowire arrays using anodic aluminum oxide templates"
PVSEC 2012.11, HangZhou, China

4. ChongE Wang, Yoshinori.Tanaka, Toshifumi Terui, Shukichi Tanaka, Tomohiro Shimizu1 and Shoso Shingubara
"Electroplating technology for the fabrication of Cu_2ZnSnS_4 nanowire arrays using anodic aluminum oxide template"
TMC 2012.12, Niigata

5. ChongE Wang, A.Kondo, T. Terui, S. Tanaka, K. Takase T. Shimizu and S. Shingubara
"Fabrication of Cu_2ZnSnS_4 thin films by sulfurization of electrodeposited CuZn/CuSn precursor layers with CS_2"

JSAP 2013.9, Kyoto

6. ChongE Wang, T. Shimizu, S. Tanaka, A Kawakami, A.Kondo, T. Terui, K. Takase and S. Shingubara
"Fabrication of Cu_2ZnSnS_4 thin films photovoltaic cell by CS_2 source sulfurization of electrodeposited stacked binary alloy layers"
PVSEC 2013.10, Taiwan

7. ChongE Wang, Akihito Kondo, Takuya Yamaguchi, Shukichi Tanaka, Yukihiro Tominari, Yasuhiro Hara, Tomohiro Shimizu and Shoso Shingubara
"Fabrication of vertical Cu2ZnSnS4/Mo/Si nanocylinder arrays using a patterned Si template"
EMRS 2014.5, France

Acknowledgement

I gratefully acknowledge all the people who contributed directly or indirectly to the accomplishment of this Ph. D work.

I would like to acknowledge my supervisor, Prof. Shoso Shingubara, for provided me the opportunity to work in his group, studying photovoltaic absorber materials, an interesting subject of great fundamental and technical importance. Under his leadership, I have been enabled to work in an active group with open and friendly atmosphere.

I also would like to acknowledge Prof. Tomohiro Shimizu, I learnt from him not only his extensive knowledge in physics and plenty of brilliant and creative ideas, but also his strict academic attitude, which will have influences on my whole life of scientific career.

I feel also grateful to Prof. Sumio Nakahara and Shigeyoshi Hisada for their kind assistance.

I would like to thank all applied physics lab members, and I am deeply grateful for their hospitality.

ChongE Wang

May 2014 Osaka, Japan